Standing on the Shoulders of Dwarfs: the Kepler Asteroseismic LEGACY Sample. II.Radii, Masses, and Ages — **Source link** ☒

Victor Silva Aguirre, Mikkel N. Lund, Mikkel N. Lund, H. M. Antia ...+30 more authors

Institutions: Aarhus University, University of Birmingham, Tata Institute of Fundamental Research, Max Planck Society
...+8 more institutions

Topics: Asteroseismology and Stars

Related papers:

- Ages and fundamental properties of Kepler exoplanet host stars from asteroseismology

- Standing on the Shoulders of Dwarfs: the Kepler Asteroseismic LEGACY Sample. I. Oscillation Mode Parameters

- Kepler Planet-Detection Mission: Introduction and First Results

- Modules for Experiments in Stellar Astrophysics (MESA)

- A new correction of stellar oscillation frequencies for near-surface effects

Standing on the shoulders of Dwarfs: the Kepler asteroseismic LEGACY sample II - radii, masses, and ages

Silva Aguirre, V.; Lund, M.~N.; Antia, H.~M.; Ball, W.~H.; Basu, S.; Christensen-Dalsgaard, J.; Lebreton, Y.; Reese, D.~R.; Verma, K.; Casagrande, L.; Justesen, A.~B.; Mosumgaard, J.~R.; Chaplin, W.~J.; Bedding, T.~R.; Davies, Guy.; Handberg, R.; Houdek, G.; Huber, D.; Kjeldsen, H.; Latham, D.~W.

Document Version
Peer reviewed version

[Link to publication on Research at Birmingham portal](#)

arXiv:1611.08776v3 [astro-ph.SR] 2 Dec 2016

STANDING ON THE SHOULDERS OF DWARFS: THE *KEPLER* ASTEROSEISMIC LEGACY SAMPLE II — RADII, MASSES, AND AGES

Víctor Silva Aguirre[1], Mikkel N. Lund[2,1], H. M. Antia[3], Warrick H. Ball[4,5], Sarbani Basu[6],
Jørgen Christensen-Dalsgaard[1], Yveline Lebreton[7,8], Daniel R. Reese[9,2,1], Kuldeep Verma[3,1],
Luca Casagrande[10], Anders B. Justesen[1], Jakob R. Mosumgaard[1], William J. Chaplin[2,1],
Timothy R. Bedding[11,1], Guy R. Davies[2,1], Rasmus Handberg[1], Günter Houdek[1], Daniel Huber[11,12,1],
Hans Kjeldsen[1], David W. Latham[13], Timothy R. White[1], Hugo R. Coelho[2], Andrea Miglio[2], and Ben Rendle[2]

[1]Stellar Astrophysics Centre, Department of Physics and Astronomy, Aarhus University, Ny Munkegade 120, DK-8000 Aarhus C, Denmark

[2]School of Physics & Astronomy, University of Birmingham, Edgbaston Park Road, West Midlands, Birmingham, UK, B15 2TT

[3]Tata Institute of Fundamental Research, Homi Bhabha Road, Mumbai 400005, India

[4]Institut für Astrophysik, Georg-August-Universität Göttingen, Friedrich-Hund-Platz 1, 37077, Göttingen, Germany

[5]Max-Planck-Institut für Sonnensystemforschung, Justus-von-Liebig-Weg 3, 37077 Göttingen, Germany

[6]Department of Astronomy, Yale University, PO Box 208101, New Haven, CT 06520-8101, USA

[7]Observatoire de Paris, GEPI, CNRS UMR 8111, F-92195 Meudon, France

[8]Institut de Physique de Rennes, Université de Rennes 1, CNRS UMR 6251, F-35042 Rennes, France

[9]LESIA, Observatoire de Paris, PSL Research University, CNRS, Sorbonne Universités, UPMC Univ. Paris 06, Univ. Paris Diderot, Sorbonne Paris Cité, 92195 Meudon, France

[10]Research School of Astronomy and Astrophysics, Mount Stromlo Observatory, The Australian National University, ACT 2611, Australia

[11]Sydney Institute for Astronomy (SIfA), School of Physics, University of Sydney, NSW 2006, Australia

[12]SETI Institute, 189 Bernardo Avenue, Mountain View, CA 94043, USA

[13]Harvard-Smithsonian Center for Astrophysics, 60 Garden Street Cambridge, MA 02138 USA

ABSTRACT

We use asteroseismic data from the *Kepler* satellite to determine fundamental stellar properties of the 66 main-sequence targets observed for at least one full year by the mission. We distributed tens of individual oscillation frequencies extracted from the time series of each star among seven modelling teams who applied different methods to determine radii, masses, and ages for all stars in the sample. Comparisons among the different results reveal a good level of agreement in all stellar properties, which is remarkable considering the variety of codes, input physics and analysis methods employed by the different teams. Average uncertainties are of the order of ∼2% in radius, ∼4% in mass, and ∼10% in age, making this the best-characterised sample of main-sequence stars available to date. Our predicted initial abundances and mixing-length parameters are checked against inferences from chemical enrichment laws $\Delta Y/\Delta Z$ and predictions from 3D atmospheric simulations. We test the accuracy of the determined stellar properties by comparing them to the Sun, angular diameter measurements, Gaia parallaxes, and binary evolution, finding excellent agreement in all cases and further confirming the robustness of asteroseismically-determined physical parameters of stars when individual frequencies of oscillation are available. Baptised as the *Kepler* dwarfs LEGACY sample, these stars are the solar-like oscillators with the best asteroseismic properties available for at least another decade. All data used in this analysis and the resulting stellar parameters are made publicly available for the community.

Keywords: Asteroseismology – stars: fundamental parameters – stars: oscillations

1. INTRODUCTION

Asteroseismology has changed the way we determine properties of stars. The detection of oscillations at the surface is a window to their interiors as they allow us to determine their physical properties with a precision that is otherwise extremely hard to achieve in field stars.

These properties, ages in particular, are crucial to our understanding of different fields of astrophysics (such as Galactic Archaeology, see e.g., Miglio et al. 2013; Casagrande et al. 2016). Stellar age determinations, by traditional means, can be very uncertain (see e.g., Soderblom 2010) and most age estimates, even when they

claim to be precise, are not necessarily accurate.

The most widely used method to obtain ages of stars is to compare their observed atmospheric properties with those predicted by theoretical evolutionary sequences (e.g., Edvardsson et al. 1993; Ng & Bertelli 1998; Pont & Eyer 2004) or theoretical isochrones in the case of star clusters. This approach works reasonably well for clusters as long as the colour-magnitude diagram is well defined and contains stars in all stages of evolution, in particular the main-sequence, the main-sequence turnoff and the red-giant branch. However, the technique of evolutionary-track or isochrone fitting does not work very well for single stars. More sophisticated statistical treatments, particularly Bayesian estimates (e.g., Jørgensen & Lindegren 2005; Takeda et al. 2007), are needed to obtain unbiased ages and, even then, uncertainties can be large. Estimating stellar ages also becomes increasingly problematic for stars that are more distant and hence fainter: reddening is uncertain, and the distances to the stars are not yet well known (although Gaia will drastically change this picture).

The CoRoT and *Kepler* missions have completely changed the field of asteroseismology. Prior to these missions, solar-like oscillations for stars other than the Sun were observed in only a small number of them (see e.g., Chaplin & Miglio 2013, for a review). Space-based photometry has now made asteroseimic analyses almost routine. The *Kepler* mission detected solar-like oscillations in hundreds of main-sequence and subgiant stars, and the global asteroseismic parameters of these targets have been used to determine properties such as mass and radius (Chaplin et al. 2014). While the mass and radius estimates of these stars are reliable, their ages are less so due to the lack of sensitivity of these global properties to the deep stellar layers, where most of the evolutionary change takes place. To overcome this and determine robust asteroseismic ages for these stars, it is necessary to extract and model the full spectrum of individual oscillation modes.

Silva Aguirre et al. (2015) and Davies et al. (2016) analysed and modelled a sample of 33 exoplanet hosts for which the *Kepler* mission had obtained asteroseismic data, including individual oscillation frequencies. Those results have informed other studies of exoplanet systems (e.g., Van Eylen & Albrecht 2015; Bonfanti et al. 2016; Jontof-Hutter et al. 2016), and of the relation between stellar rotation and age (van Saders et al. 2016). In this paper we perform a similar analysis to that of Silva Aguirre et al. (2015) for a set of 66 main-sequence stars observed by *Kepler* that are not known to be exoplanet hosts. Instead, the target stars are selected as those with the highest signal-to-noise ratios and the most precisely determined oscillation frequencies. In recent years there have been similar studies using smaller sam-

ples and observation of shorter duration (e.g., Appourchaux et al. 2012; Mathur et al. 2012; Metcalfe et al. 2014). The dataset used for this work has been extracted from the full available set of observations made by the *Kepler* mission, which for most stars means frequencies obtained from a four-year time series. Thus, the targets comprising this study, which we baptise as the *Kepler* dwarfs LEGACY sample, have the best asteroseismic data available among solar-like stars for at least another decade (i.e., until the PLATO 2.0 mission, Rauer et al. (2014)).

The companion paper by Lund et al. 2016 (submitted) describes the details of the data analysis and the frequencies that have been used in the modelling presented in this study. The rest of this paper is organised as follows. In Section 2 we describe the selection criteria for choosing the sample of stars that have been analysed. We also discuss the ancillary data such as effective temperatures and metallicity needed for the analysis. The different techniques used in modelling the stars are described in Section 3. Section 4 is devoted to the results of the analysis, and tests of the derived properties using independent constraints are given in Section 5. We summarise the results and mention some of their applications in Section 6.

2. THE LEGACY SAMPLE

Our goal was to select main-sequence stars of the highest asteroseismic data quality present in the *Kepler* sample. A thorough description of the selection process and the main observational properties of our targets are given in the accompanying paper by Lund et al. 2016 (submitted). We give a brief account of the most important points in this section.

The 66 stars comprising the LEGACY sample were chosen from more than 500 main-sequence and subgiant targets in which *Kepler* detected oscillations (Chaplin et al. 2014). We selected all targets that had more than one year of short-cadence observations, and where inspection of the power spectrum did not reveal any clear signature of bumped $\ell = 1$ modes. These are modes of mixed character that behave like pressure modes in the envelope and buoyancy modes in the core, and their appearance is related to the end of the core-hydrogen burning phase (Aizenman et al. 1977).

Figure 1 shows an asteroseismic Hertzsprung-Russell diagram (HRD) where the luminosity on the y-axis has been replaced by an asteroseismic property known as the average large frequency separation. This quantity decreases as stars evolve, since it is approximately proportional to the square root of the mean stellar density (Ulrich 1986; Gough 1987):

$$\langle \Delta\nu \rangle \propto \left(\frac{M}{M_\odot} \right)^{1/2} \left(\frac{R}{R_\odot} \right)^{-3/2} . \tag{1}$$
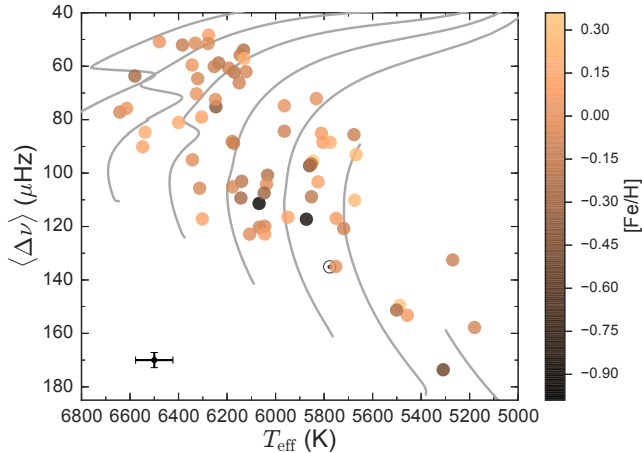
Figure 1. Position of the LEGACY sample (filled circles) and the Sun in an asteroseismic HRD, colour coded according to their surface chemical composition. Typical error bar in effective temperature and large frequency separation is shown in black. Also depicted are representative stellar evolution tracks at solar metallicity spanning a mass range between $0.8-1.4\,\mathrm{M}_\odot$ in steps of $0.1\,\mathrm{M}_\odot$ (from Silva Aguirre et al. 2015). As a side note we mention that the two lowest mass tracks do not evolve further into the red giant phase as the computations where stopped at an age of 16 Gyr.

The large frequency separation in Fig. 1 has been determined for the data using a gaussian-weighted linear fit to the $\ell = 0$ frequencies as a function of radial order as described in Lund et al. 2016 (submitted). Tracks at solar metallicity are shown in the figure as a reference, depicting the evolution of solar-type stars in this parameter space. Our sample predominantly comprises stars hotter and more evolved than the Sun, an expected bias since the amplitudes of oscillations scale approximately with stellar luminosity (Kjeldsen & Bedding 1995), making their detection easier in that region of the asteroseismic HRD. The atmospheric composition of our targets spans values from super-solar metallicity at $[\mathrm{Fe/H}] = 0.35$ to metal-poor stars of $[\mathrm{Fe/H}] = -1.00$, making this sample the most extended one in terms of heavy-element abundances where a homogeneous asteroseismic analysis is feasible using individual frequencies of oscillation. A summary of the global asteroseismic quantities and atmospheric properties of the sample as compiled for this modelling effort is given in Appendix B.

3. ASTEROSEISMIC MODELLING PIPELINES

Seven independent pipelines were used to determine the stellar properties of the LEGACY sample. These pipelines use a variety of evolutionary and pulsation codes and consider different sets of input physics when computing theoretical evolutionary sequences and oscil-

lation frequencies. Moreover, each pipeline uses its own preferred set of asteroseismic observables and statistical approach to analyse the goodness of fit of the models and extract the stellar properties of each target. In the following we give a brief general description of the common characteristics in the process of estimating stellar properties from asteroseismic modelling, and give the specific details of each pipeline in an itemised list below.

Firstly, one must generate a set of stellar models for different masses and chemical compositions using a stellar evolution code and set of input physics. Next, for many of these models theoretical oscillation frequencies are computed using a standard (adiabatic) pulsation code. The actual number of evolutionary models and frequencies calculated is either defined in advance (when pipelines use precomputed grids of models) or determined during the fitting process (when pipelines chose masses and composition as part of the optimisation). In both cases, the net result is stellar structures with atmospheric properties and theoretically computed frequencies that can be compared to those obtained from observations.

All pipelines use the atmospheric parameters T_{eff} and $[\mathrm{Fe/H}]$ as constraints but there are variations in the way asteroseismic data are used when determining stellar properties. One method is to fit the individual oscillation frequencies, $\nu_i(n)$, using a suitable prescription to correct for the surface effect (see e.g., Kjeldsen et al. 2008; Ball & Gizon 2014; Sonoi et al. 2015, for a physical motivation and description of these corrections). Another method is to fit combinations of frequencies, normally the frequency separation ratios, defined as (Roxburgh & Vorontsov 2003):

$$r_{02}(n) = \frac{d_{02}(n)}{\Delta\nu_1(n)} \quad (2)$$

$$r_{01}(n) = \frac{d_{01}(n)}{\Delta\nu_1(n)}, \; r_{10}(n) = \frac{d_{10}(n)}{\Delta\nu_0(n+1)}. \quad (3)$$

Here, $\Delta\nu_\ell(n) = \nu_{n,\ell} - \nu_{n-1,\ell}$ is the large separation between modes of same angular degree and consecutive overtone, $d_{02}(n) = \nu_{n,0} - \nu_{n-1,2}$ is the small frequency separation, and $d_{01}(n)$ and $d_{10}(n)$ are the 5-point small frequency separations:

$$d_{01}(n) = \frac{1}{8}(\nu_{n-1,0} - 4\nu_{n-1,1} + 6\nu_{n,0} - 4\nu_{n,1} + \nu_{n+1,0}) \quad (4)$$

$$d_{10}(n) = -\frac{1}{8}(\nu_{n-1,1} - 4\nu_{n,0} + 6\nu_{n,1} - 4\nu_{n+1,0} + \nu_{n+1,1}). \quad (5)$$

The frequency separation ratios have been shown to be mostly sensitive to the deep layers of the star (see e.g., Roxburgh 2005; Otí Floranes et al. 2005; Silva Aguirre et al. 2011a), effectively diminishing the impact of poor modelling of the stellar outer layers in 1D evolutionary

codes as well as the requirement of line-of-sight velocity corrections (see, Davies et al. 2014). Due to the strong correlations between combinations including five individual frequencies, the ratios are customarily written and reproduced as one unique set of observables, called r_{010} (see, e.g., Silva Aguirre et al. 2013):

$$r_{010} = \{r_{01}(n), r_{10}(n), r_{01}(n+1), r_{10}(n+1), ...\}. \quad (6)$$

The pipelines participating in this study use individual frequencies, or combinations of frequencies, or both, following their own preference.

The process of determining stellar properties can be computationally expensive, since some methods produce individual grids for each of the fitted targets that can require calculating thousands of models and frequencies for a given set of input physics. The inclusion of additional physical processes such as microscopic diffusion or overshooting effectively increases the grid-dimensions to explore and can lead to a rapid increase in the number of models required to properly sample the parameter space. One alternative used by some pipelines to reduce the computational load is to use the average large frequency separation $\langle\Delta\nu\rangle$ and the frequency of maximum power in the oscillation spectrum $\nu_{\max}$ as physically motivated proxies to constrain the parameter space that needs to be covered by the models. Since these quantities are sensitive to the mean stellar density and surface gravity, respectively (Ulrich 1986; Brown et al. 1991), they can restrict the mass and radius combinations that need to be explored.

All modelling teams were provided with the global asteroseismic parameters ($\langle\Delta\nu\rangle$ and $\nu_{\max}$), the individual frequencies, frequency ratios, and correlations as determined by Lund et al. 2016 (submitted), as well as the atmospheric properties $T_{\rm eff}$ and [Fe/H] compiled from the literature. For most of our targets, the effective temperature and composition were taken from the spectroscopic analysis made by Buchhave & Latham (2015), and for the remainder we opted for other sources compiled from the literature. Table 3 reports the values given to the modelling teams, including the references for the atmospheric properties used.

In the following, we describe the main characteristics of the seven pipelines employed in the analysis and enclose a summary of them in Table 1.

AIMS The "Asteroseismic Inference on a Massive Scale" pipeline is described in detail for the first time in this paper and we give a description of it in Appendix A. Briefly, it uses the grid of MESA models from Coelho et al. (2015) and Delaunay tessellation for linear interpolation across the grid. It then applies an MCMC algorithm to find a representative set of models which satisfy the seismic and classic constraints. Stellar properties and uncertainties

are obtained by averaging and calculating the standard deviations of the properties from the set of models.

ASTFIT The "ASTEC FITting" method uses the ASTEC evolutionary code (Christensen-Dalsgaard 2008b) coupled to ADIPLS (Christensen-Dalsgaard 2008a) for computation of theoretical pulsation frequencies in a grid of stellar models. The initial chemical composition is determined exploring a range of values for the galactic enrichment law, and it includes the effects of microscopic diffusion for low-mass stars and three values of the mixing-length efficiency $\alpha_{\rm MLT} = 1.5, 1.8, 2.1$. The statistical methods applied to determine the stellar properties are described in Appendix A1 of Silva Aguirre et al. (2015).

BASTA The "BAyesian STellar Algorithm" uses precomputed grids of evolutionary models and performs a global search for the optimal solution using the Bayesian approach described by Silva Aguirre et al. (2015). The current implementation considers microscopic diffusion for masses below 1.2 $M_\odot$, and the NACRE rates with the updated $^{14}N(p,\gamma)^{15}O$ reaction from Formicola et al. (2004), and overshooting in the exponential decay formulation of Freytag et al. (1996) using the calibrated efficiency determined by Magic et al. (2010). The original grids have been extended in this work to include lower metallicities as required to match the spectroscopically determined surface composition of some targets.

C2kSMO The "Cesam2k Stellar Model Optimization" pipeline (C2kSMO) uses the Cesam2k evolutionary code coupled to the Liège Oscillations Code and the procedures described by Lebreton & Goupil (2014). The input physics considered includes atomic diffusion, convective core overshooting with an efficiency of $d_{\rm ov} = 0.15 \times \min(H_{\rm p}, R_{\rm convcore})$, convection being treated under the Canuto et al. (1996) formalism, and the NACRE rates with the updated $^{14}N(p,\gamma)^{15}O$ reaction from Imbriani et al. (2005). An initial approach to the solution is performed by finding the best fit to the observed values of $T_{\rm eff}$, [Fe/H], and $\log(g)$ (the latter obtained from the global asteroseismic parameter $\nu_{\max}$), using a chemical enrichment law $\Delta Y/\Delta Z$ from a solar calibration computed with the same input physics. The resulting age, mass and initial chemical composition are used as starting values in a Levenberg-Marquardt minimisation that adjusts free parameters in the modelling in order to minimise the merit function (see Miglio & Montalbán 2005). These free model parameters are the age and mass of the star, the initial helium content and initial $(Z/X)_0$ ratio, and the convective efficiency $\alpha_{\rm CGM}$. The observables fitted by this optimisation process are [Fe/H], $T_{\rm eff}$, $\log(g)$, the lowest observed radial mode, and the frequency separation ratios r_{010} and r_{02}. The error bars on the free

Table 1. Summary of codes, input physics and optimisation methods applied by each pipeline.

	AIMS	ASTFIT	BASTA	C2kSMO
Models	MESA	ASTEC	GARSTEC	Cesam2k
Frequencies	InversionKit	ADIPLS	ADIPLS	LOSC
Solar Mixture	GN93	GN93	GS98	GN93
Opacities	OPAL96+JF05	OPAL96+JF05	OPAL96+JF05	OPAL96+JF05
EOS	OPAL05	OPAL05	OPAL05	OPAL05
Nuclear Reactions	NACRE	NACRE	NACRE	NACRE
Atmosphere	Eddington grey	Eddington grey	Eddington grey	Eddington grey
Diffusion	No	MP93, ≤ 1.1 M$_\odot$	T94, ≤ 1.2 M$_\odot$	MP93
Overshoot	Yes	No	Yes	Yes
Convection	CG68	MTL58	MLT12	CGM96
$\alpha_{\rm conv}$	1.8	1.5, 1.8, 2.1	1.791	Variable
$\Delta Y/\Delta Z$	2.0	1.0-2.0	1.4	Variable
Fitted data	$\nu_i(n)$	$\nu_i(n)$	$r_{010}, r_{02}(n)$	$r_{010}, r_{02}(n), \nu_0(n_{\rm min})$
Surface correction	BG14	SC	None	TS15
Optimisation	MCMC	χ^2 minimization	Bayesian	Levenberg-Marquardt
Reference	Appendix A	VSA15	VSA15	LG14

GOE	V&A	YMCM
MESA	MESA	YREC
ADIPLS	ADIPLS	AB94
GS98	GS98	GS98
OPAL96+JF05	OP05+JF05	OPAL96+JF05
OPAL05	OPAL05	OPAL05
NACRE	NACRE	Solar Fusion
Eddington grey	Eddington grey	Eddington grey
T94	T94, ≤ 1.35 M$_\odot$	No
Yes	Yes	Yes
CG68	MLT58	MTL58
Variable	Variable	Variable
Variable	Variable	Variable
$\nu_i(n)$	$\langle\Delta\nu\rangle, \langle r_{02}\rangle, r_{01}(n), r_{10}(n+3)$	$\nu_i(n), r_{010}, r_{02}(n)$
BG14	HK08	BG14
Downhill simplex	χ^2 minimization	Monte Carlo
TA15	TA15	VSA15

NOTE—References. Evolutionary models: ASTEC (Christensen-Dalsgaard 2008b), Cesam2k (Morel & Lebreton 2008), GARSTEC (Weiss & Schlattl 2008), MESA (Paxton et al. 2011), YREC (Demarque et al. 2008). Pulsation frequencies: AB94 (Antia & Basu 1994), ADIPLS Christensen-Dalsgaard (2008a), LOSC Scuflaire et al. (2008). Solar mixture: GN93 (Grevesse & Noels 1993), GS98 (Grevesse & Sauval 1998). Opacities: OPAL96 (Iglesias & Rogers 1996), OP05 (Badnell et al. 2005), JF05 (Ferguson et al. 2005). Equation of state (EOS): OPAL05 (Rogers & Nayfonov 2002). Nuclear reactions: Solar Fusion (Adelberger et al. 1998), NACRE (Angulo et al. 1999). Convection theory: MLT58 (Böhm-Vitense 1958), CG68 (Cox & Giuli 1968), MLT12 (Kippenhahn et al. 2012), CGM96 (Canuto et al. 1996). Diffusion: T94 (Thoul et al. 1994), MP93 (Michaud & Proffitt 1993). Surface corrections: HK08 (Kjeldsen et al. 2008), SC (solar scaled, see appendix A1 in Silva Aguirre et al. 2015), BG14 (Ball & Gizon 2014), TS15 (Sonoi et al. 2015). Pipelines: VSA15 (Silva Aguirre et al. 2015), LG14 (Lebreton & Goupil 2014), TA15 (Appourchaux et al. 2015). See text for details.

parameters are obtained as the diagonal coefficients of the inverse of the Hessian matrix, while uncertainties in the other parameters are obtained following Eq. 10 in Deheuvels et al. (2016).

GOE The setting of the "GOEttingen" pipeline is very similar to that described by Appourchaux et al. (2015) and Reese et al. (2016). Since more massive stars are included in the LEGACY sample, the Ledoux (1947) criterion for convection was used with an extra free parameter for the convective overshooting described according to the exponential model of Freytag et al. (1996). The NACRE thermonuclear reactions are used with the updated rates in $^{14}N(p,\gamma)^{15}O$ from Imbriani et al. (2005). The free adjustable parameters to find the best-fitting

model were age, initial metallicity, initial helium, the mixing-length, the overshooting efficiency, and the two terms in the Ball & Gizon (2014) surface correction.

V&A This approach uses a combination of the MESA and ADIPLS codes to compute evolutionary models and pulsation frequencies with the same input physics as listed in Table 3 of Appourchaux et al. (2015). Diffusion of helium and heavy elements is typically not included for stars with masses greater than 1.35 $M_\odot$, while overshoot is taken into account with an exponentially decaying efficiency for stars in the relevant mass regime (above 1.10 $M_\odot$). For thermonuclear reactions the NACRE compilation is used with the exception of updated rates in the $^{14}N(p,\gamma)^{15}O$ reaction from Imbriani et al. (2005). The properties of stars are determined via χ^2 minimization over a suitable grid of models. This is the only pipeline that uses the large frequency separation as an asteroseismic constraint, obtained by a linear least-squares fit to the observed frequencies as a function of radial order.

YMCM The "Yale Monte Carlo Method" is applied as described by Silva Aguirre et al. (2015), with the exceptions of a variable value of the mixing-length parameter and the use of the Ball & Gizon (2014) formulation to correct for surface effects. The Solar fusion (Adelberger et al. 1998) cross section for $^{14}N(p,\gamma)^{15}O$ has been updated according to Formicola et al. (2004).

4. RESULTS

4.1. *Precision of the stellar properties*

We determined stellar properties for the 66 stars in the LEGACY sample using the pipelines described in the previous section. Considering the variety of methods and input physics involved in the process, we choose to report the results from all of pipelines in complete and homogeneous sets given in Appendix C.

Figure 2 shows the uncertainty distributions obtained by each pipeline for the LEGACY sample. Overall, the results agree at the level of the size of their formal uncertainties, with some exceptions for given parameters. In terms of formal errors in density the BASTA results are of the order ∼2.5%, a factor of two larger than the majority of pipelines, while uncertainties from C2kSMO have median values at the 16% level and are much larger than those of any other pipeline. The reasons for these discrepancies are related to the details of each individual method: BASTA is the only pipeline to fit only frequency ratios, which are less sensitive to the mean density of the star than individual frequencies (see Silva Aguirre et al. 2015, for a discussion). On the other hand, the local minimisation Levenberg-Marquardt algorithm used by C2kSMO does not determine uncertainties for density so these are derived by (uncorrelated) error propagation

from mass and radius, which results in much higher formal errors than all other methods.

In Fig. 2, the results for radius and mass also reveal some differences between the pipelines: C2kSMO has much larger radius uncertainties and formal mass errors only slightly smaller than the rest of the methods, resulting in the large density fractional uncertainties. Age distributions show some pipelines with fractional errors below 10% (C2kSMO and GOE) while the rest encompass values between 10-30%, which is in much better agreement with the level of age uncertainties determined from hare-and-hounds exercises (Reese et al. 2016) and those normally obtained from individual frequency fitting of *Kepler* main-sequence targets (e.g., Mathur et al. 2012; Silva Aguirre et al. 2013; Lund et al. 2014; Lebreton & Goupil 2014; Silva Aguirre et al. 2015).

The distributions in age show a tail towards large fractional error values (up to ∼60%), much higher than the expected formal uncertainties from asteroseismic determinations. These are dominated by the youngest stars in our sample that have statistical errors of similar magnitude than the oldest stars. A more physically motivated scale to compare the age uncertainty distributions is given by the Terminal Age Main Sequence (TAMS), which we define as the point where the remaining central hydrogen content in a stellar model reaches 1×10^{-5}. Five pipelines were able to produce a proxy for the TAMS values of our targets by evolving their best-fitting model beyond the main-sequence phase. Figure 3 shows the uncertainty distributions normalised by current and TAMS age, where the tail at large fractional uncertainties is clearly reduced by the change in scale while the peak of the distribution remains very close to its original value. The latter is a consequence of an asteroseismic detection bias which favours more evolved stars, as the oscillation amplitudes scale proportionally with stellar luminosity (e.g., Kjeldsen & Bedding 1995).

In summary, stellar properties of our targets are determined to varying degrees of precision by the pipelines, with median uncertainties ranging from 0.5%−2.6% in density (excluding the C2kSMO results, see above); 1.3%−4.2% in radius; 2.3%−4.5% in mass; and 6.7%−20% in age. This level of precision is comparable to previous asteroseismic studies of smaller samples using individual frequencies of oscillations, and makes this set the best-characterised main-sequence sample from the nominal *Kepler* mission.

4.2. *Comparison between pipelines*

The stellar properties predicted by each pipeline represent an estimate of the true physical parameters of our sample based on a given set of data. For the large majority of our targets, we lack an independent verification of these stellar properties that would allow us to test the va-
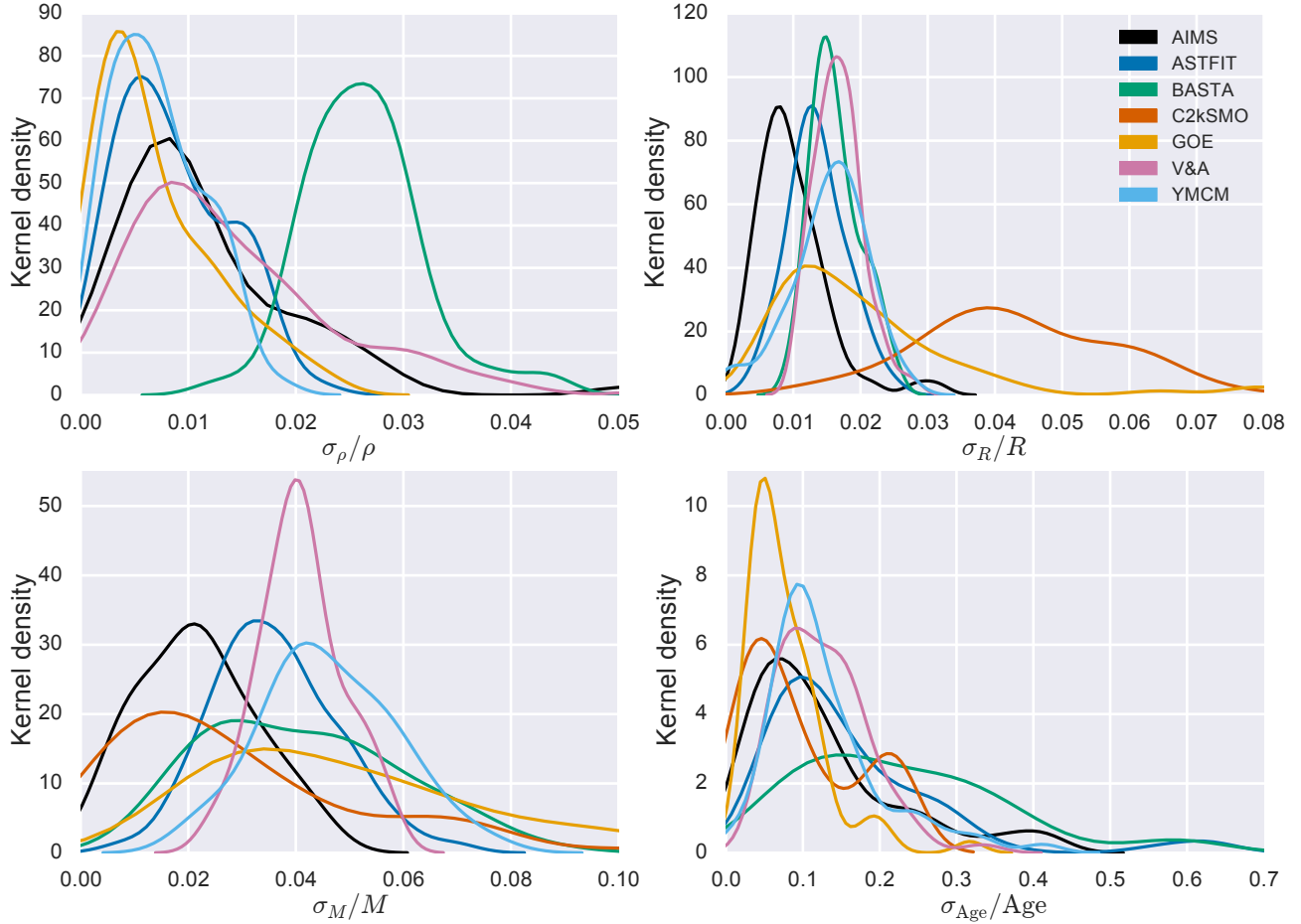
Figure 2. Distribution of uncertainties in density, radius, mass, and age for all stars in the sample as determined by each pipeline. When asymmetric error bars are reported these were added in quadrature for the figure. Values for the `C2kSMO` density uncertainties are beyond the scale of the plot and therefore not shown. See text for details.
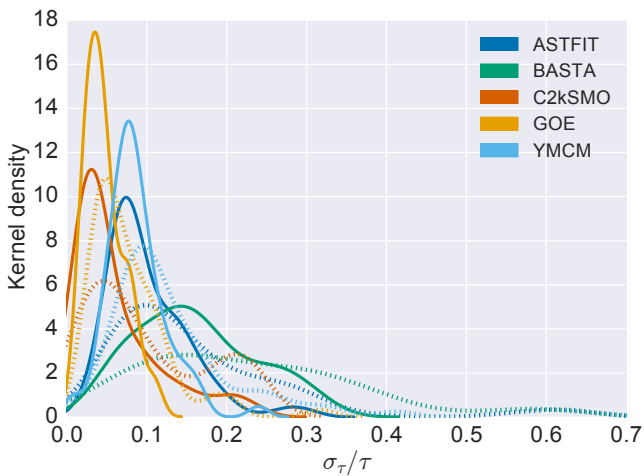

Figure 3. Age uncertainty distributions normalised to the TAMS age (solid) or the seismically determined age (dotted) of the target. See text for details.

ceptions). It is customary in these cases to compare the results across methods by selecting a reference pipeline and plot the fractional differences in a given quantity as a function of the result predicted by the reference. Since *a priori* we cannot consider any set of results to be an accurate representation of the underlying stellar properties of the sample, this approach can introduce spurious correlations misleading the analysis (see, e.g., Ludbrook 1997). An alternative is to use the Altman-Blandt method for analysing differences (Bland & Altman 1986, 1995), consisting in calculating the actual difference between the results of a pipeline and the reference, and plotting them against the corresponding mean values. Figures 4, 5, 6, and 7 depict these differences for density, radius, mass, and age using the `BASTA` results as a reference. In each panel we include the results of computing the Pearson product-moment correlation coefficient r of the mean values, as well as the p-value of a one-sample $t-$test of the weighted mean of the differences.

If there is no proportional bias between the results of a

lidity of our results (but see Section 5 below for some ex-
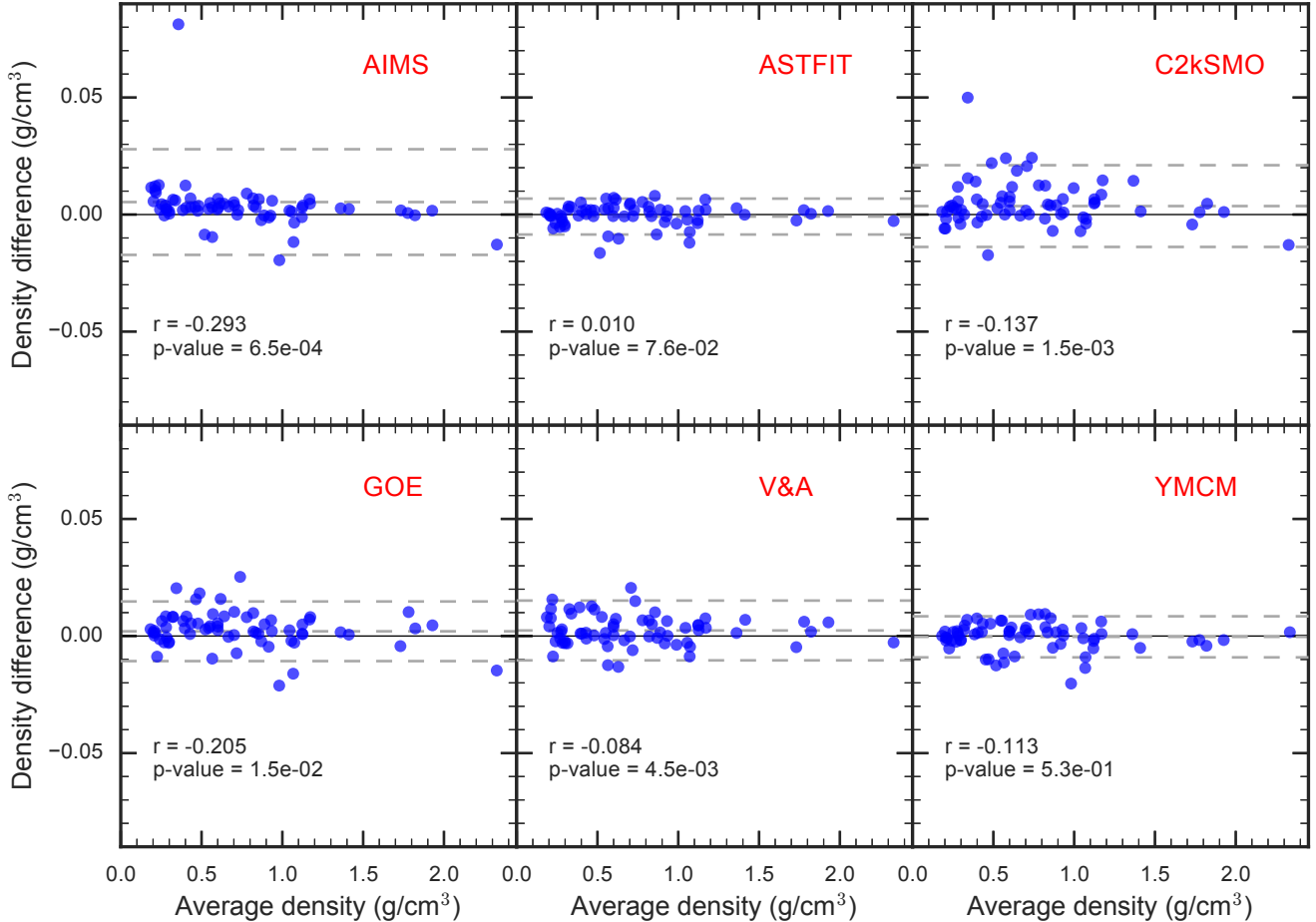
Figure 4. Densities determined from each pipeline compared to those obtained with `BASTA`. The abscissa shows the average density value calculated between the pipeline and `BASTA` while the ordinate gives the density differences in the sense (pipeline−`BASTA`). Solid lines mark the zero level to guide the eye while dashed lines correspond to the mean and twice the standard deviation of the differences weighted by their uncertainties (added in quadrature). Pearson correlation coefficients r and p-values are also given. See text for details.

pipeline and the reference, the regression of the difference on means should have a slope of zero. For a sample of the size considered here, it translates into an absolute value of $|r| > 0.25$ for the bias to be significant at the 5% level. Except for the `AIMS` comparison, r values in Fig. 4 reveal no proportional bias in density as a function of its mean value, a reassuring result considering that the large frequency separation is reproduced by all methods when fitting individual frequencies and it scales to good approximation with the square root of the mean stellar density (see Eq. 1).

We include in the comparison plots dashed lines showing the mean and twice the standard deviation of the differences (weighted by the uncertainties). If there were no fixed bias between the results then the mean of the differences should be zero. To test this, we performed a one-sample t−test of the weighted mean of the difference in each stellar property, where resulting p-values below

0.05 reject the H_0 hypothesis of zero mean differences and reveal a fixed bias between the methods. Thus, we find no such biases in the comparisons with `ASTFIT`, and `YMCM`, while the other four pipelines show a statistically significant (and positive) fixed bias.

To gain further understanding of these results we followed up with a similar analysis of the results for radius and mass, showed in Figs. 5 and 6. There is a clear proportional bias in radius between `BASTA` and `ASTFIT` (increasing), and between `BASTA` and `V&A` (decreasing). Considering that this correlation was not observed in any pipeline for the density results, it must be compensated in the mass determinations as confirmed by Fig. 6 where the same two pipelines show a proportional bias according to their r values. On the other hand, the proportional bias in density between `BASTA` and `AIMS` is a result of a similar bias in radius, as the mass comparison between these pipelines shows no traces of such bias.

The results of the t-test for radius revealed a fixed bias for `C2kSMO` and `YMCM`, both cases predicting larger radii than `BASTA`. In the case of `C2kSMO` a similar behaviour was already present in the density: since this pipeline extracts this quantity from propagation of the mass and radius determinations we expected one of these quantities to be the underlying effect causing the bias. The mass comparison does not show a fixed bias between `C2kSMO` and `BASTA`.

Masses determined with `YMCM` are the only ones showing a statistically significant fixed bias (higher values), while the `ASTFIT` and `V&A` results hint towards proportional biases in mass (cf, Fig. 6). One would naively expect a similar behaviour in the age determination, since mass is the main property controlling the main-sequence lifetime of a star. Figure 7 reveals that there are no correlations as a function of age for any of the pipeline results, and also that the fixed bias between `BASTA` and `YMCM` is not significant. However, only `C2kSMO` and `YMCM` do not show a significant fixed bias while all other pipelines do predict such a difference. The lack of correspondence between masses and ages is a result of the differences in evolutionary and pulsation codes employed by the methods, as well as the included input physics (see Table 1, also the discussion in Sect. 4 of Silva Aguirre et al. 2015).

In summary, the results from different pipelines show some fixed and proportional biases for given stellar properties, but overall there is an excellent level of agreement considering the variety of evolutionary and pulsation codes, input physics employed, as well as the differences in the seismic quantities fitted by each pipeline. This heterogeneity across methods as seen from Table 1 makes it difficult to isolate the unique physical culprit of a particular outlier in our sample. Thus, we have focused our comparison on general trends with description of individual cases when possible, and note that detailed discussions of the impact of changing the input physics on asteroseismically derived properties are given by Lebreton & Goupil (2014) and Silva Aguirre et al. (2015).

4.3. *Initial helium abundance and mixing-length parameter*

Four of the pipelines used in our analysis include initial abundances and efficiency of convection as free parameters that are determined during the optimisation process. We can therefore compare the resulting values with expectations based on chemical enrichment of the Galaxy and predictions of 3D hydrodynamical simulation of atmospheres.

One of the most poorly constrained ingredients in modelling solar-type stars is the helium content, as its abundance cannot be determined from spectroscopic observa-

tions. The transformation from the observed metallicity [Fe/H] to fractional abundances X, Y, Z is achieved by assuming a relation between heavy elements and helium content known as the chemical enrichment law $\Delta Y/\Delta Z$. The existence and value of such a relation have long been debated, and current understanding favours the range between $1 \leq \Delta Y/\Delta Z \leq 3$ as obtained from different sets of indicators (see e.g., Lebreton et al. 1999; Jimenez 2003; Balser 2006; Casagrande et al. 2007; Serenelli & Basu 2010, and references therein). The relation is anchored to a known point in the helium-heavy elements plane, normally the values obtained from Standard Big Bang Nucleosynthesis (SBBN) calculations $Z_0 = 0$ and $Y_0 = 0.248$ (Steigman 2010).

Figure 8 shows the initial helium and heavy element abundance for all targets as predicted by the four pipelines freely varying the composition as part of the optimisation. All panels show cases where Y_{ini} is below the measurement from SBBN, a problem commonly appearing in asteroseismic results fitting individual oscillation frequencies (see e.g., Mathur et al. 2012; Metcalfe et al. 2014; Silva Aguirre et al. 2015).

A linear fit to the results from each pipeline (weighted by the uncertainties when available) shows slopes compatible with the broad range of $1 \leq \Delta Y/\Delta Z \leq 3$ for the `C2kSMO` and `GOE` pipelines, while the fit to the `V&A` predictions returns a slightly lower slope. The `YMCM` abundances cluster systematically below the $\Delta Y/\Delta Z = 1$ line and in combination with sub-SBBN helium for its most metal-poor stars predict the highest slope of all targets.

Despite the aforementioned differences, the overall asteroseismic predictions are broadly consistent with the slopes commonly adopted as galactic chemical enrichment laws. The recent measurement of surface helium abundance using asteroseismology in the binary 16 Cyg A&B (Verma et al. 2014b) and the detection of glitches associated with the HeII ionisation zone in all stars from our sample (Verma et al. 2016, submitted) open the possibility for detailed studies that can potentially put firm constraints on Y_{ini}, and it will be pursued in a future study.

Another poorly constrained parameter that has a huge impact in the modelling results of solar-type stars is the efficiency of convection, parameterised in both the mixing-length (Böhm-Vitense 1958) and the full spectrum of turbulent eddies (Canuto et al. 1996) theories. Normally this efficiency is calibrated to the Sun and used across the HRD, but asteroseismic fitting allows us to obtain a determination of this parameter by including it in the optimisation process. These predictions have not been tested to date due to the lack of benchmarks for comparison, but a new approach is now possible by extracting information about convective efficiency from large grids of 3D hydrodynamical simulations of stellar
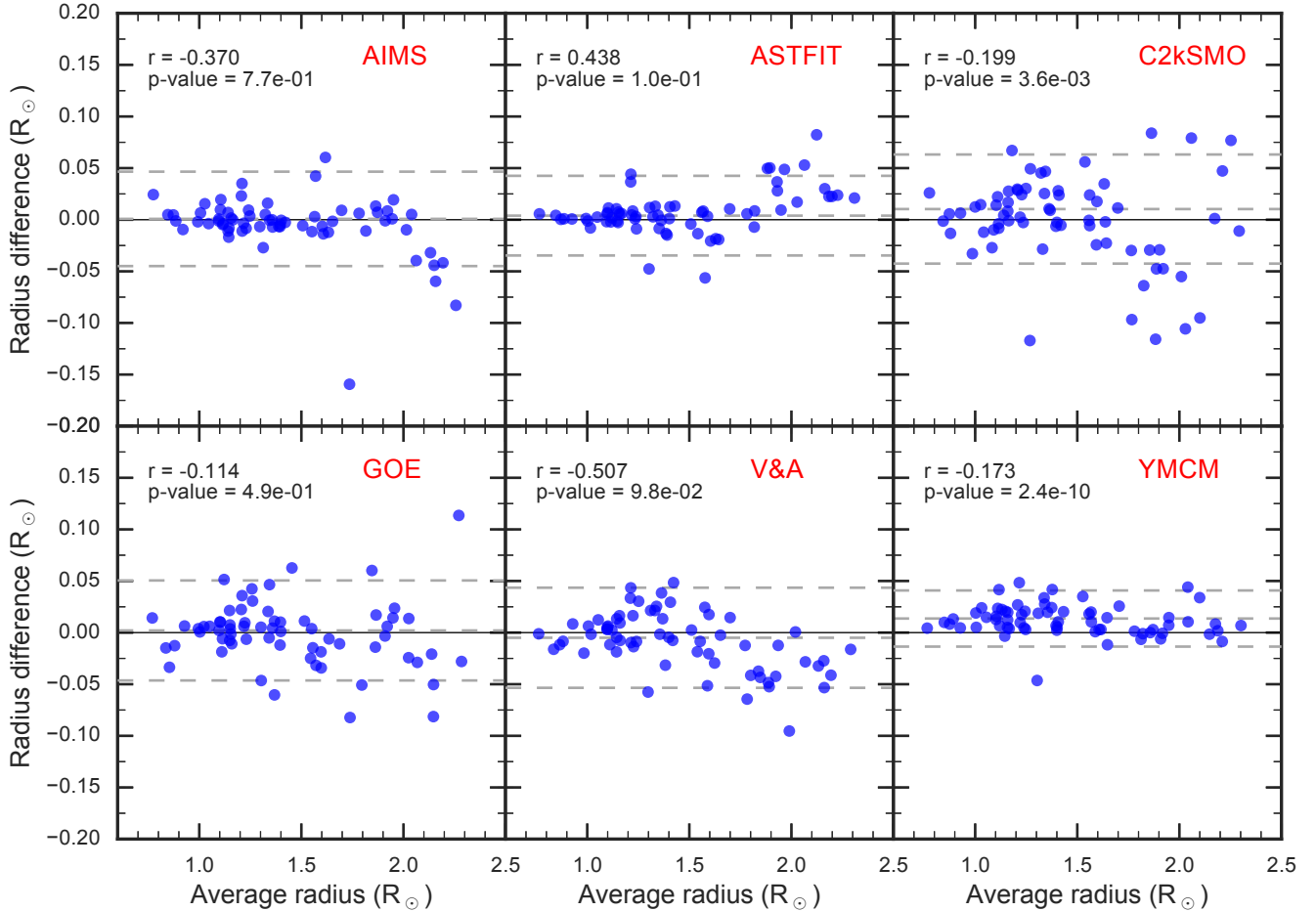
Figure 5. Same as figure 4 but for radius determinations.

atmospheres. These simulations follow the properties of convection in the outer stellar layers without the need of free parameters, and can be used to calibrate the expected mixing-length parameter by matching a 1D envelope model to a suitable average of the 3D simulations (see Trampedach et al. 2014; Magic et al. 2015, for a description of the procedure).

In particular, the Stagger collaboration has produced a grid of more than 200 simulations covering a wide range in metallicity, effective temperature and surface gravity. An equivalent mixing-length parameter based on these 3D simulations is available as a function of these properties (Magic et al. 2015), and we make a first comparison of their results to our determinations in Fig. 9. For a given pipeline we show, as a function of $T_{\rm eff}$, the ratio between the mixing-length parameter of each star and the value for the Sun obtained from a solar calibration. In the 3D hydrodynamical case, the solar value is determined from an average solar simulation. The rationale behind presenting the comparison in terms of ratios in the convective efficiency is to minimise as much as possible the effects of the different input physics used in each

pipeline and the atmospheric simulations. We caution that the comparison with C2kSMO is shown only for guidance, as this pipelines uses the Canuto et al. (1996) theory for convection whose efficiency value is not directly comparable to the mixing-length one.

None of the pipelines in our study follow the decreasing trend in convective efficiency as a function of $T_{\rm eff}$ predicted by the simulations. In fact, two of the pipelines are consistent with a relatively flat relation (C2kSMO and V&A), while the GOE and YMCM pipelines seem to suggest the opposite behaviour as the observed in the 3D case. It is worth noticing that V&A predicts mixing-length parameters systematically lower than the solar one. The results from 3D simulations in terms of an HRD-position-dependent convective efficiency are starting to be adopted by the stellar community in evolutionary calculations (see, e.g., Salaris & Cassisi 2015; Mosumgaard et al. 2016, for the first examples), and our sample of stars would be perfectly suited to test the impact of including results from 3D simulations on asteroseismically derived properties.
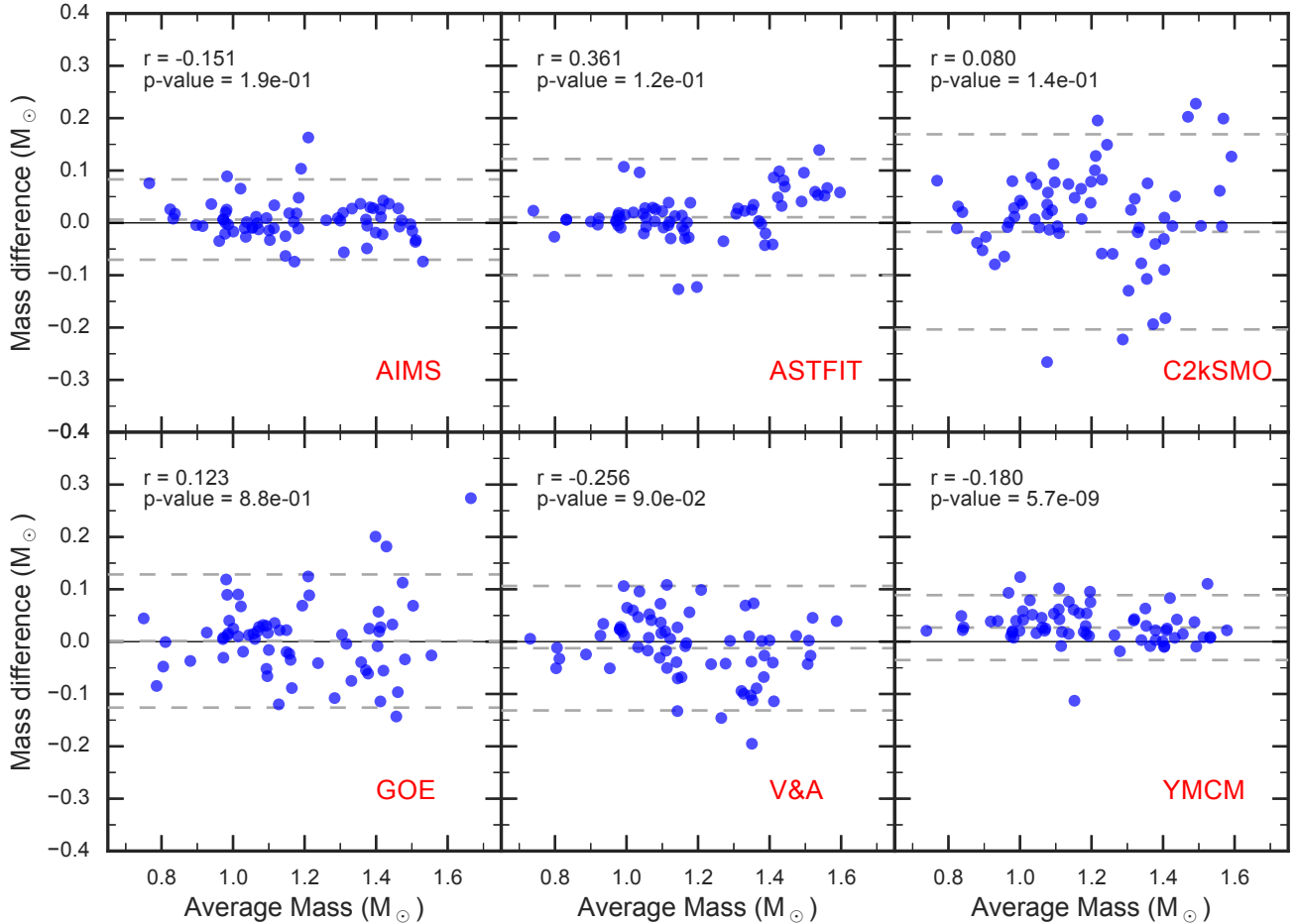
Figure 6. Same as figure 4 but for mass determinations.

5. ACCURACY OF STELLAR PROPERTIES

In the previous section we compared the results from the different pipelines assuming that the real values of the predicted stellar properties were not known, and therefore each determination of a given quantity was treated as an independent method of measurement. While this is true for the large majority of our targets, in some cases additional constraints on the stellar properties are available from interferometry, parallaxes, or binarity. The following sections put our derived quantities under scrutiny using these additional data.

5.1. *The Sun*

Our own sun is the star we have best characterised in the Universe and displays a rich spectrum of stochastically-excited modes of oscillations. To test the accuracy of our pipelines we included in the target list circulated among all modellers a set of frequencies determined from solar data degraded in quality to match that of the *Kepler* mission (see Lund et al. 2016, submitted, for details). The true identity of this star was concealed from the modellers, and the results presented here in-

clude the same relevant input physics as given in Table 1 and fitting methods described in Sec 3. Besides the frequencies, we provided a temperature of $T_{\rm eff} = 5752 \pm 77$ K and a surface composition of [Fe/H] $= -0.02 \pm 0.15$ dex determined from a random realisation of Gaussian noise perturbations of the solar values and having uncertainties representative of the rest of the *Kepler* LEGACY sample. The results are given in Table 2 and shown in Fig. 10, showing that in general most methods return values compatible with the solar properties. However, some discrepant results appear that deserve further discussion.

The mass reported by C2kSMO are more than 3σ away from the Sun despite determining values comparable to other pipelines that agree with solar properties within one standard deviation. The reason is the smaller uncertainties in this parameter returned by this method, a feature which was already visible in relation to Fig. 2. A similar issue is found in the derived mass and radius from AIMS, where the results lie around 2σ away from the true values. It is interesting to see the impact of diffusion on the solar age: while two methods (C2kSMO and YMCM) predict central masses higher than 1 M$_\odot$, the age of the
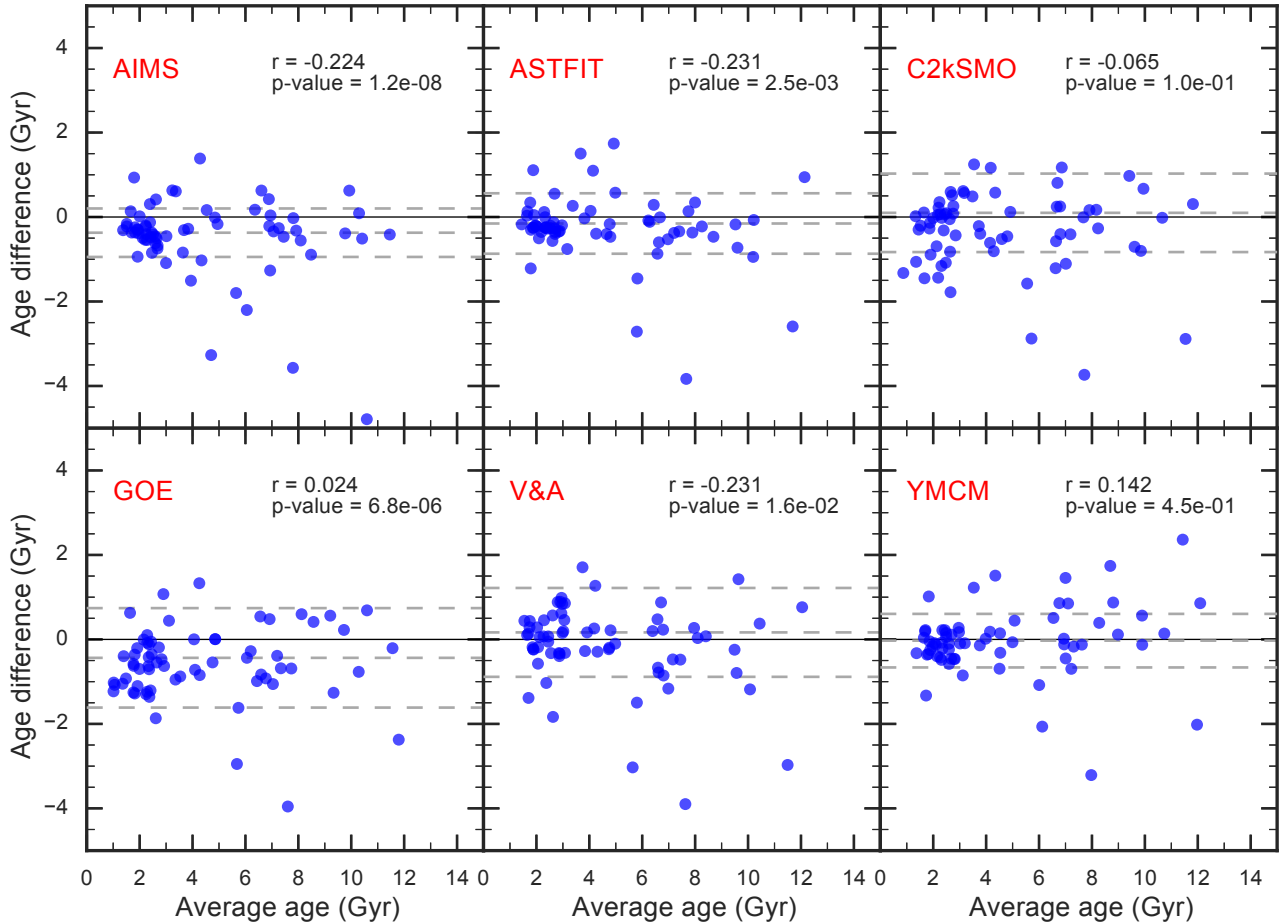
Figure 7. Same as figure 4 but for age determinations.

latter is not lower than the solar one due to the lack of microscopic diffusion in the modelling (see Table 1). A test including this effect in the `YMCM` modelling results in an estimated age of $\tau = 4.83$ Gyr, in better agreement with the solar value of 4.57 Gyr.

The solar properties determined by the `V&A` method favour a sub-solar mass and a surface helium abundance higher than measured by helioseismology (see Table 2). This anti-correlation between mass and helium is expected from homology relations (e.g., Weiss et al. 2005) and has been reported before in asteroseismic modelling methods using local optimisation (e.g, Mathur et al. (2012); Metcalfe et al. (2014), see also Section 4.3 in Lebreton & Goupil (2014) and Section 4.4 in Silva Aguirre et al. (2015)).

According to homology relations there is a strong dependence of the stellar luminosity on the mean molecular weight. Since the luminosity is related to the effective temperature and radius, once these are determined there is a narrow range of combinations of mass and helium abundance that can comply with this constraint. The `V&A` results for the Sun reveal a bimodal distribution in

mass, and the most probably of these peaks is reported in Table 2. However, the secondary solution is in better agreement with the solar properties, yielding a mass of 1.036 $M_\odot$ and surface helium of $Y_{sup} = 0.237$. We note that when comparing the two solutions, the secondary one cannot be ruled out at the 2σ level, and analysis of the amplitude of frequency glitches in the spectrum as done by Verma et al. (2014b,a) favours the high-mass results. This type of study can help breaking the degeneracy between mass and helium abundance and will be considered it a subsequent paper.

Finally we turn to parameters that have been successfully determined from helioseismic inferences, namely the depth of the convective envelope and the helium surface abundance (see Christensen-Dalsgaard 2002, for a review). In both cases, all but the `V&A` results give agreement within 1σ to the helioseismic values, giving us confidence about the stellar parameters determined from these techniques for stars like the Sun.

5.2. *Interferometry and photometry*

Independent radius determinations provide another check on the stellar properties derived from astero-
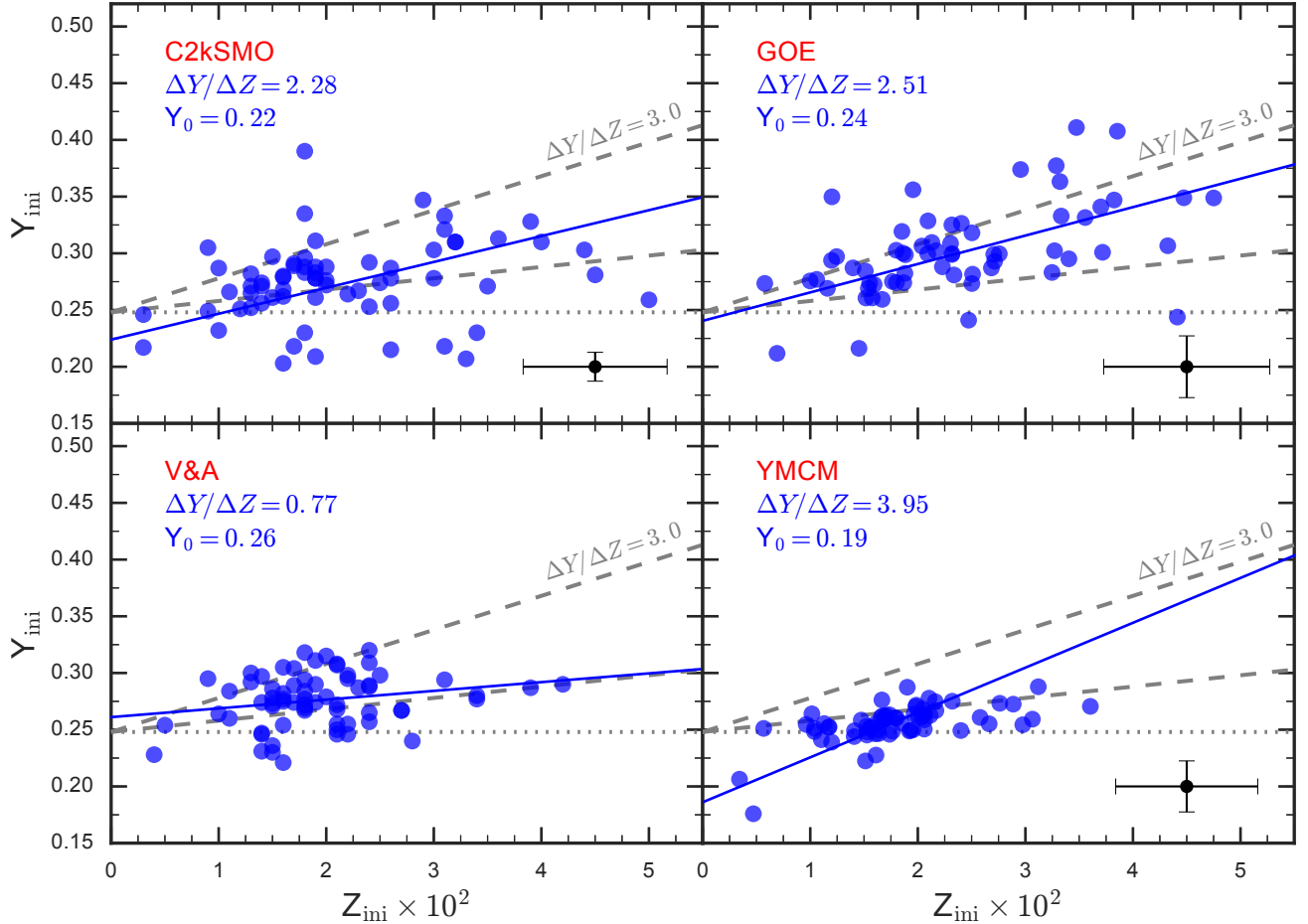
Figure 8. Initial helium abundance as a function of initial heavy elements abundance for the pipelines that do not constrain the chemical composition with a galactic enrichment law. Two dashed grey lines depict different slopes in the $\Delta Y/\Delta Z$ relation: 3.0 (upper), 1.0 (lower). The dotted grey line shows the primordial helium abundance predicted by SBBN (Steigman 2010), while the solid blue lines present a linear least-square fit to the results from each pipeline, characterised by the slope and intercept given in each panel. Median uncertainties are plotted to avoid clutter (black circles, except for V&A that does not provide them for these parameters). See text for details.

seismology. Results from interferometric campaigns with CHARA combined with Hipparcos parallaxes have started to appear for targets where oscillations have been detected by *Kepler*, but currently amount to a handful in the main-sequence and red giant phases (Huber et al. 2012; White et al. 2013; Johnson et al. 2014). In fact, only five of our targets have published interferometric radii that we can compare to the determinations from asteroseismology.

Figure 11 shows the results for the binary 16 Cyg A&B (White et al. 2013) and KIC 8006161 (Huber et al. 2012). For all three there is very good agreement between interferometric and asteroseismic radii, except for the AIMS results, which are more than 1σ away from the observations in two cases. For the other two stars in our sample that have interferometric radii, the comparison is shown in Fig. 12. There is a clear difference between

the radius from CHARA and the asteroseismically determined ones, the latter being systematically smaller. However, these stars have the smallest angular diameters measured in the Huber et al. (2012) sample (0.289 and 0.231 mas), making them more prone to systematic errors in the adopted calibrator diameters than for larger target stars which are better resolved. In light of this, we restrict the comparison with interferometry to stars with angular diameters larger than > 0.3 mas and also consider another independent radius determination coming from the InfraRed Flux Method (IRFM).

In the implementation considered here, the IRFM used several photometric bands to determine the bolometric flux of a star and its effective temperature in a self-consistent manner (see Casagrande et al. 2010, 2014b, and Section 5.3 below for details). A natural by-product of this procedure is the stellar angular diameter which,
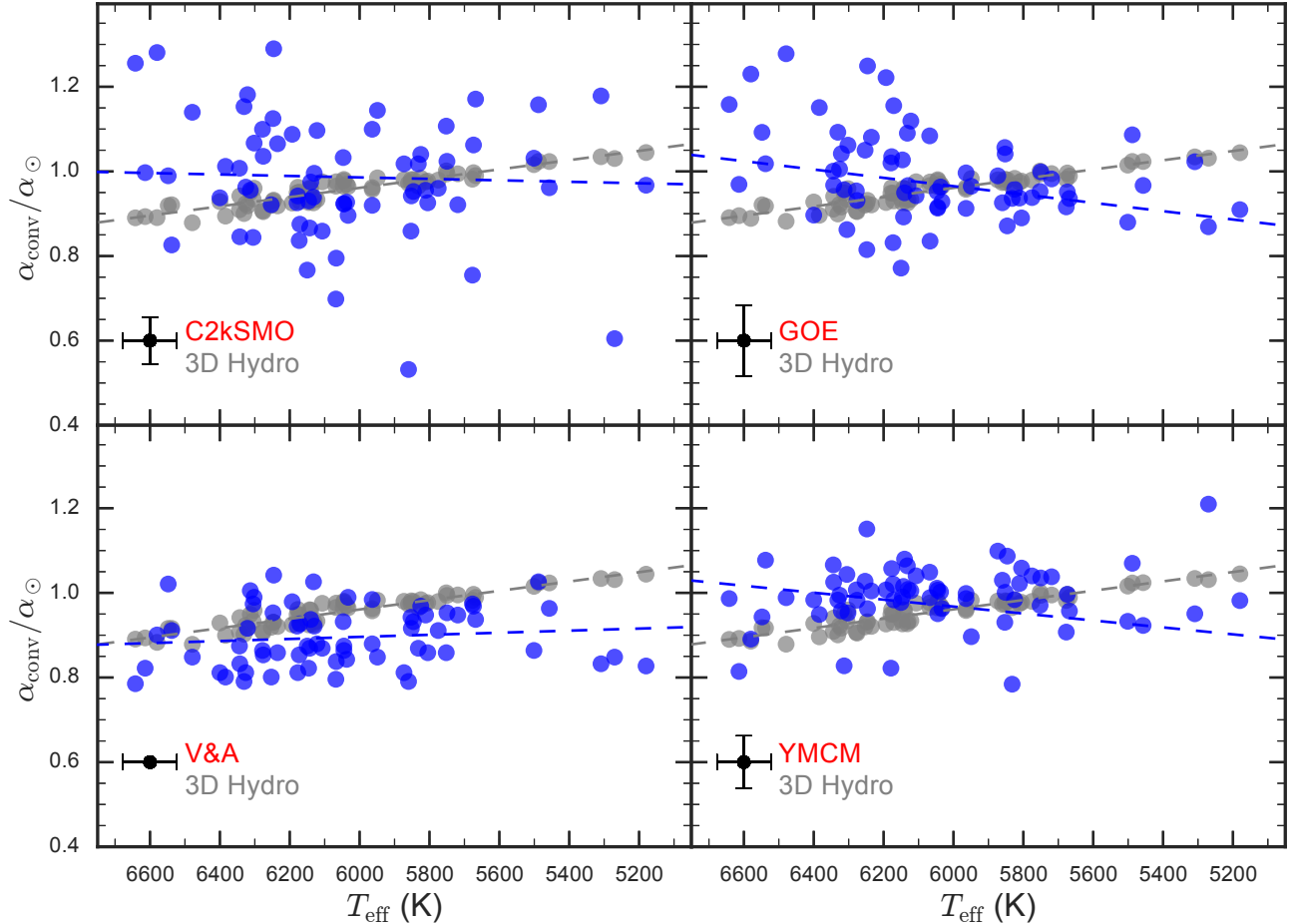
Figure 9. Mixing-length parameter as a function of effective temperature for the LEGACY sample. Plotted on the Y-axis is the ratio between the α parameter of the targets and the solar mixing length determined for each pipeline (blue circles) or from 3D hydrodynamical simulations (grey circles). Dashed lines represent a linear fit weighted by the uncertainties when available. To avoid clutter, median uncertainties from each pipeline are plotted (black circles). The `C2kSMO` results are computed with the Canuto et al. (1996) formalism of convection. See text for details.

combined with parallax measurements, yields stellar radius as depicted in Fig. 12.

The agreement with asteroseismic radii is better than the comparison with interferometry, suggesting that the differences with the interferometric results indeed come from calibration problems. Additionally, the interferometric effective temperatures for these two targets are lower (by $1-2\sigma$) than the IRFM and spectroscopic temperatures presented in this work and from Bruntt et al. (2012), translating into systematic differences of the order of ~3%. Only additional data from CHARA or another interferometer in the future will yield further information about these discrepancies, but we can conclude that the current available observations support the accuracy of asteroseismic radius determinations for these five targets. We note in passing that the IRFM results for KIC 8006161and 16 Cyg A&B also agree well with the predictions from all pipelines.

5.3. Parallaxes

Using parallaxes to test the accuracy of asteroseismic results is a less direct method of comparison than e.g., radius determination from interferometry. The measured parallaxes can accurately determine the distance to our targets, which in turn can be predicted from asteroseismic radii if an estimate of the stellar angular diameter is available. Now that the Gaia mission has provided parallaxes for all stars in common with the Hipparcos and Tycho-2 catalogues (Lindegren et al. 2016), we can compare our distance determinations for 64 of the targets appearing in the Gaia data release 1 (DR1, Gaia Collaboration et al. 2016).

We base our asteroseismic distance determinations on a method that couples radii to IRFM results in a self-consistent manner, as described by Silva Aguirre et al. (2011b, 2012). Briefly, the bolometric flux (and therefore angular diameter) was estimated from Tycho and

Table 2. Solar properties determined from each pipeline. See text for details.

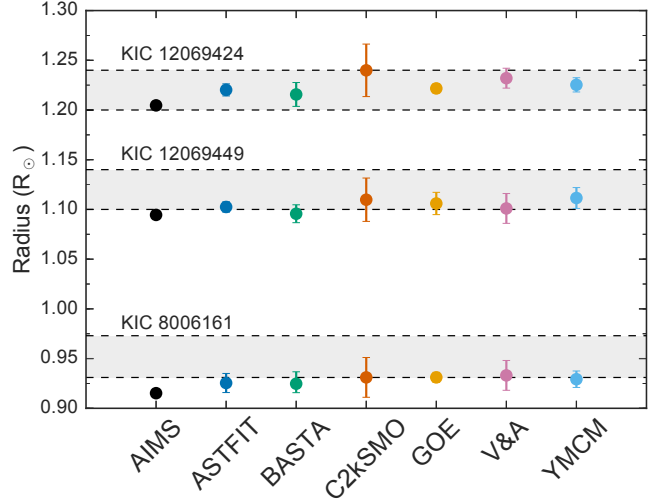|	Mass ($M_\odot$)	Radius ($R_\odot$)	Age (Myr)	Luminosity ($L_\odot$)	Density (g/cm^3)	Y_{sup}	R_{BCZ} ($R_\odot$)
AIMS	0.979 ± 0.013	0.992 ± 0.005	4840 ± 367	1.060 ± 0.048	1.413 ± 0.004	–	–
ASTFIT	0.986 ± 0.023	0.994 ± 0.008	4686 ± 393	0.972 ± 0.052	1.411 ± 0.003	0.249 ± 0.009	0.71 ± 0.007
BASTA	$0.978^{+0.039}_{-0.030}$	$0.993^{+0.012}_{-0.012}$	4852^{+1181}_{-1069}	$0.976^{+0.054}_{-0.052}$	$1.411^{+0.021}_{-0.022}$	$0.247^{+0.012}_{-0.01}$	$0.713^{+0.009}_{-0.009}$
C2kSMO	1.021 ± 0.003	1.006 ± 0.010	$4331 \pm 85.$	1.084 ± 0.048	1.412 ± 0.048	0.245 ± 0.003	0.715 ± 0.004
GOE	0.997 ± 0.006	0.995 ± 0.018	4859 ± 128	0.947 ± 0.041	1.412 ± 0.002	0.234 ± 0.009	0.720 ± 0.003
V&A	0.927 ± 0.030	0.973 ± 0.015	4621 ± 200	0.937	1.418 ± 0.006	0.277	0.725
YMCM	$1.037^{+0.031}_{-0.047}$	$1.012^{+0.005}_{-0.005}$	5297^{+350}_{-350}	$1.008^{+0.043}_{-0.042}$	$1.406^{+0.001}_{-0.001}$	$0.248^{+0.01}_{-0.01}$	$0.716^{+0.003}_{-0.003}$

NOTE—The surface helium abundance (Y_{sup}) and radius of the base of the convective envelope (R_{BCZ}) are not determined by AIMS, while V&A reports only values from the best fit model (and thus no uncertainties) for these parameters and the luminosity. For reference, the solar age is determined to be 4.57 Gyr (Bahcall et al. 1995) while helioseismology predicts $Y_{sup} = 0.248 \pm 0.003$ (Basu 1998) and $R_{BCZ} = 0.713 \pm 0.001$ $R_\odot$ (Christensen-Dalsgaard et al. 1991)
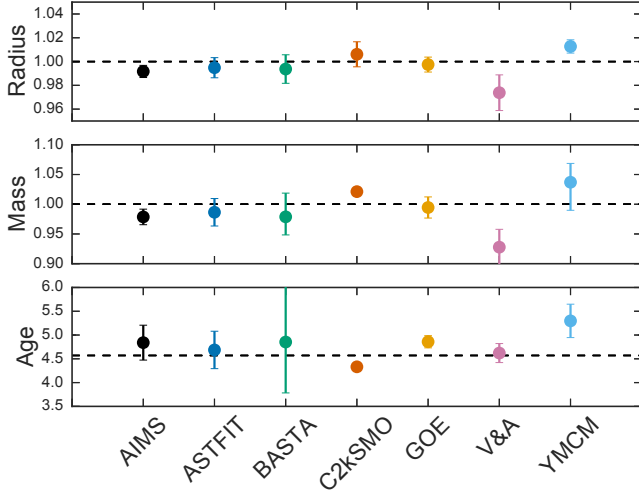
Figure 10. The radius, mass, and age of the Sun determined by the pipelines for the concealed solar dataset. See text for details.

Figure 11. Comparison of interferometric radii from Huber et al. (2012) (KIC 8006161) and White et al. (2013) (16 Cyg A&B, KIC 12069424 and KIC 12069449) with those determined seismically by each pipeline. Grey shaded areas and horizontal dashed lines depict the standard deviation reported in the interferometric measurements.

2MASS photometry using the spectroscopic metallicity of each star and a reddening value given by the distance dependent map of Amôres & Lépine (2005). We then interpolated using the asteroseismic gravity determined by each pipeline to extract a value of angular diameter and estimate its distance using the radius. We have assumed a uniform uncertainty in angular diameter of 3% (see Casagrande et al. 2014a, for further details on the implementation adopted). The resulting asteroseismic distances have median uncertainties of the order of 4.5%, while the median astrometric parallax uncertainty from the Gaia DR1 is close to 1%.

The resulting comparison is presented in Fig. 13 where we plot the distribution of normalised differences between the asteroseismically determined distance transformed to parallax and the measurements from Gaia. There is an overall good level of agreement between all seismic pipelines, but an offset at the level of 1σ appears when comparing to the results of DR1 (with the astro-

metric parallax being systematically smaller than those predicted by asteroseismology). A similar result has recently been found by Stassun & Torres (2016) who compared Gaia distances with independent measurements from eclipsing binaries, and found a constant offset of −0.25 mas in the sense of Gaia parallaxes being too small. The right panel in Fig. 13 shows the comparison of our distances with those corrected by the constant offset found by Stassun & Torres (2016) where it is clear that the results agree much better if this systematic shift is applied. We note that 20 of our stars are also present in the Hipparcos catalogue and had asteroseismic distances available (from Silva Aguirre et al. 2012) which were recently compared to Gaia results by De Ridder et al. (2016). The authors conclude that there is excel-
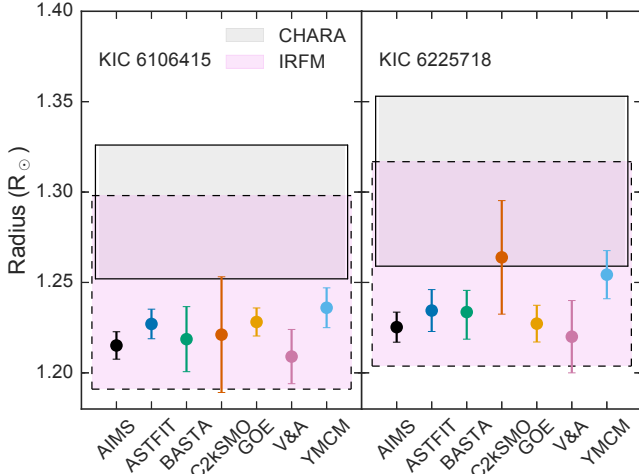
Figure 12. Same as Fig. 11 showing the interferometric radius from Huber et al. (2012) (grey shaded region and solid lines) and the radius determined using the IRFM formulation from Casagrande et al. (2014b) (violet shaded region and dashed lines). See text for details.

lent agreement between the new astrometric and asteroseismic parallaxes, but there is a small offset pointing towards Gaia parallaxes being too small although within the uncertainties in the determinations (similar to what is found here, see Fig. 2 in De Ridder et al. 2016).
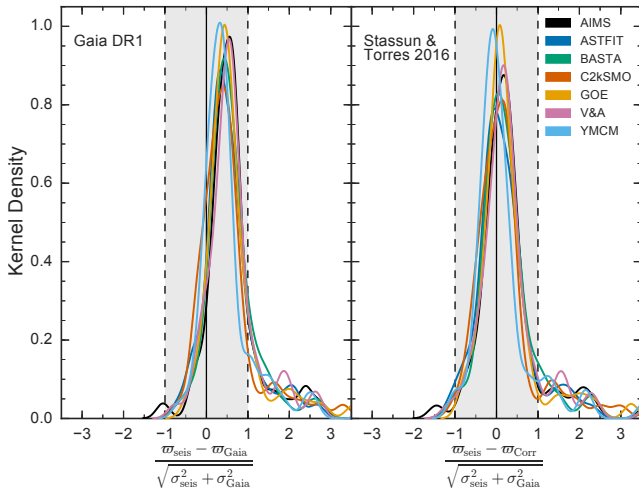
Figure 13. Comparison of parallaxes determined from asteroseismic distances and those measured by the Gaia satellite. Each panel shows the distribution of the difference between both determinations normalised by the individual uncertainties. Grey shaded area and vertical dashed lines mark the 1σ region. *Left:* using parallaxes directly from Gaia DR1. *Right:* applying the Stassun & Torres (2016) correction to the Gaia parallaxes. See text for details.

Although it is tempting to corroborate the conclusion

of Gaia predicting too long distances drawn by Stassun & Torres (2016) from our sample, we note that there are other factors that could lie at the foundation of the systematic offset observed in the distances. For instance, our results and the properties of the eclipsing binaries used by Stassun & Torres (2016) depend on the adopted temperature scale. If our implementation of the IRFM were to return hotter temperatures and therefore smaller angular diameters, that would result in smaller radii and therefore larger distances and could potentially solve this discrepancy. Further analysis goes beyond the scope of this paper and will be presented for larger samples in upcoming studies (Huber et al., in preparation; Sahlholdt et al., in preparation). We also mention that an uncertainty of 0.3 mas is quoted in the Gaia DR1 as systematic which is of the same order as the one found here (Gaia Collaboration et al. 2016).

Despite the overall good agreement between asteroseismic and astrometric parallaxes, some outliers remain beyond the 3σ level. Reasons that could explain this discrepancy are contaminated photometry compromising the IRFM determinations of angular diameters, inaccurate reddening estimates in the 3D dust maps, or problems with the astrometric solution used to derive parallaxes. The cases of KIC 8379927 and KIC 7510397 are examples of the latter as they are known binary stars with their fluxes affected by the presence of a companion. Similarly, the targets KIC 10454113 and KIC 9025370 have only recently been identified as spectroscopic binaries based on HARPS-N data (P. E. Nissen, private communication). There are two other binary systems in our parallax sample, namely 16 Cyg A&B (KIC 12069424 and KIC 12069449) and the common proper motion pair KIC 9139151 and KIC 9139163 (Halbwachs 1986). However, the components of these systems have wide orbital separations and can be individually resolved in photometry, so there is no reason to doubt the reliability of their parallaxes and IRFM estimates of angular diameters.

There seems to be photometric contamination in KIC 1435467 (a rotationally variable star, see Ceillier et al. (2015)) and KIC 7940546 (a magnetically active star presenting flares in its light curve, see Balona (2015)). In the same vein, KIC 12317678 is an interesting case as it shows an infrared excess in its photometry attributed to circumstellar matter (McDonald et al. 2012) that could affect the fluxes used by the IRFM to extract the angular diameter. On the other hand, the parallax listed in Gaia DR1 is not consistent within the uncertainties with the value measured by the Hipparcos satellite. We expect that future data releases from Gaia will help clarify this situation. KIC 4914923 and KIC 9965715 also present deviations beyond the 3σ level that are currently attributed to problems in the reddening estimation. The remaining stars, which account for 55 out of

the 64 targets with Gaia parallaxes, have no warning flag in their photometry and show an excellent agreement in distances, confirming the reliability of asteroseismically determined radii.

5.4. *Binaries*

One final consistency check on the seismic results can be extracted from information on known binaries in our sample. Two stars in our sample have a binary companion that has either no oscillations detected (KIC 8379927) or only global seismic parameters have been extracted in one of the components (KIC 7510397, Appourchaux et al. 2015). We are therefore left with two systems: KIC 12069424−12069449 (16 Cyg A&B) and KIC 9139151−9139163. Unfortunately there are no dynamical masses derived for either of these pairs, but the fact each system was presumably formed at the same time allows us to put strong constraint on the age of the systems.

None of the pipelines participating in this work forced the ages of these binaries to match, and Fig. 14 shows the results for the two systems included in our sample. All methods return compatible results for 16 Cyg A&B, while GOE is the only outlier in the results for the other two stars (at the 1.5σ level). All considered, age determinations from all pipelines are consistent for the binaries in our sample and provide further support for the accuracy of asteroseismically determined ages from individual frequencies in main-sequence stars.
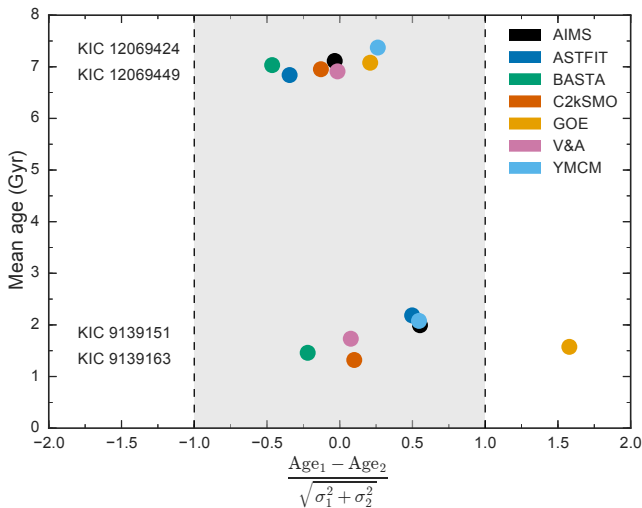
Figure 14. Ages from binary stars with both components included in our sample. Plotted in the x-axis are the age differences for both components normalised by the uncertainties, while the average age of the components is plotted in the y-axis. Grey shaded region and vertical dashed lines mark the 1σ level.

6. CONCLUSIONS AND OUTLOOK

We have presented an asteroseismic analysis for the *Kepler* dwarfs LEGACY sample, comprising main-sequence stars observed for more than a year for which individual oscillation frequencies have been detected. Using seven independent modelling pipelines we have determined precise physical properties for the 66 stars in the set, with average uncertainties of the order of $\sim 2\%$ in radius, $\sim 4\%$ in mass, and $\sim 10\%$ in age. Comparison of the results across pipelines shows a good level of agreement in the derived properties, with differences at the level expected from the variety of codes and input physics that were used in the present analysis.

Our results were subject to tests using available independent measurements of stellar properties such as those of the Sun, radii from interferometry and the IRFM, and distances from parallaxes. We found that the asteroseismically-inferred properties can reproduce the large majority of independent constraints within the uncertainties, while the deviating results can be understood in terms of stellar evolution relations (such as the mass-initial helium abundance anti-correlation) and different issues with the complementary data needed to estimate the desired property (such as contaminated photometric fluxes). These comparisons serve as confirmation of the accuracy of asteroseismic properties determined by fitting individual oscillations frequencies (or combinations thereof).

The stellar and oscillation mode properties presented here and in the accompanying paper by Lund et al. (2016, submitted) constitute the largest sample of asteroseismically-analysed main-sequence stars using individual oscillation frequencies. Adding the stars studied by Davies et al. (2016) and Silva Aguirre et al. (2015) gives 99 stars that comprise the best-characterised set of main-sequence solar-like oscillators observed by the *Kepler* mission. We have compared of our determined initial abundances with expectations from galactic chemical enrichment, and of our obtained efficiencies of convection with predictions from 3D hydrodynamical simulations. In both cases we found interesting features that motivate further study, such as sub-SBBN initial helium abundances and the non-dependance of the convective efficiency on stellar effective temperature. We make these results available for the community and hope they will provide the basis of extensive work going beyond our analysis, such as studies of convective envelopes (Mazumdar et al. 2014), surface helium abundance (Verma et al. 2014b), core convection (e.g., Deheuvels et al. 2016), inversion of the stellar interior (e.g., Buldgen et al. 2015a,b), amplitudes and line widths (e.g., Houdek et al. 2016, in preparation), average 3D simulations (e.g., Sonoi et al. 2015; Ball et al. 2016), and many

others.

REFERENCES

Adelberger, E. G., Austin, S. M., Bahcall, J. N., et al. 1998, RvMP, 70, 1265

Aizenman, M., Smeyers, P., & Weigert, A. 1977, A&A, 58, 41

Amôres, E. B., & Lépine, J. R. D. 2005, The Astronomical Journal, 130, 659

Angulo, C., Arnould, M., Rayet, M., et al. 1999, Nuclear Physics A, 656, 3

Antia, H. M., & Basu, S. 1994, A&AS, 107, 421

Appourchaux, T., Chaplin, W. J., García, R. A., et al. 2012, A&A, 543, A54

Appourchaux, T., Antia, H. M., Ball, W., et al. 2015, Astronomy and Astrophysics, 582, A25

Badnell, N. R., Bautista, M. A., Butler, K., et al. 2005, Monthly Notices of the Royal Astronomical Society, 360, 458

Bahcall, J. N., Pinsonneault, M. H., & Wasserburg, G. J. 1995, RvMP, 67, 781

Ball, W. H., Beeck, B., Cameron, R. H., & Gizon, L. 2016, Astronomy and Astrophysics, 592, A159

Ball, W. H., & Gizon, L. 2014, Astronomy and Astrophysics, 568, A123

Balona, L. A. 2015, Monthly Notices of the Royal Astronomical Society, 447, 2714

Balser, D. S. 2006, The Astronomical Journal, 132, 2326

Basu, S. 1998, MNRAS, 298, 719

Bland, J. M., & Altman, D. G. 1986, Lancet (London, England), 1, 307

—. 1995, Lancet (London, England), 346, 1085

Böhm-Vitense, E. 1958, Zeitschrift für Astrophysik, 46, 108

Bonfanti, A., Ortolani, S., & Nascimbeni, V. 2016, Astronomy and Astrophysics, 585, A5

Brown, T. M., Gilliland, R. L., Noyes, R. W., & Ramsey, L. W. 1991, ApJ, 368, 599

Bruntt, H., Basu, S., Smalley, B., et al. 2012, Monthly Notices of the Royal Astronomical Society, 423, 122

Buchhave, L. A., & Latham, D. W. 2015, The Astrophysical Journal, 808, 1

Buldgen, G., Reese, D. R., & Dupret, M. A. 2015a, Astronomy and Astrophysics, 583, A62

Buldgen, G., Reese, D. R., Dupret, M. A., & Samadi, R. 2015b, Astronomy and Astrophysics, 574, A42

Canuto, V. M., Goldman, I., & Mazzitelli, I. 1996, ApJ, 473, 550

Casagrande, L., Flynn, C., Portinari, L., Girardi, L., & Jimenez, R. 2007, MNRAS, 382, 1516

Casagrande, L., Ramírez, I., Meléndez, J., Bessell, M., & Asplund, M. 2010, A&A, 512, 54

Casagrande, L., Silva Aguirre, V., Stello, D., et al. 2014a, The Astrophysical Journal, 787, 110

Casagrande, L., Portinari, L., Glass, I. S., et al. 2014b, Monthly Notices of the Royal Astronomical Society, 439, 2060

Casagrande, L., Silva Aguirre, V., Schlesinger, K. J., et al. 2016, Monthly Notices of the Royal Astronomical Society, 455, 987

Ceillier, T., van Saders, J., García, R. A., et al. 2015, Monthly Notices of the Royal Astronomical Society, 456, 119

Chaplin, W. J., & Miglio, A. 2013, Annual Review of Astronomy and Astrophysics, 51, 353

Chaplin, W. J., Basu, S., Huber, D., et al. 2014, The Astrophysical Journal Supplement Series, 210, 1

Chiosi, C., & Matteucci, F. M. 1982, Astronomy and Astrophysics, 105, 140

Christensen-Dalsgaard, J. 2002, Reviews of Modern Physics, 74, 1073

—. 2008a, Ap&SS, 316, 113

—. 2008b, Ap&SS, 316, 13

Christensen-Dalsgaard, J., Gough, D. O., & Thompson, M. J. 1991, ApJ, 378, 413

Coelho, H. R., Chaplin, W. J., Basu, S., et al. 2015, Monthly Notices of the Royal Astronomical Society, 451, 3011

Cox, J.-P., & Giuli, R. T. 1968, Principles of stellar structure

Cyburt, R. H., Fields, B. D., & Olive, K. A. 2003, Physics Letters B, 567, 227

Davies, G. R., Handberg, R., Miglio, A., et al. 2014, Monthly Notices of the Royal Astronomical Society: Letters, 445, L94

Davies, G. R., Aguirre, V. S., Bedding, T. R., et al. 2016, Monthly Notices of the Royal Astronomical Society, 456, 2183

De Ridder, J., Molenberghs, G., Eyer, L., & Aerts, C. 2016, Astronomy and Astrophysics, 595, L3

Deheuvels, S., Brandão, I., Silva Aguirre, V., et al. 2016, Astronomy and Astrophysics, 589, A93

Demarque, P., Guenther, D. B., Li, L. H., Mazumdar, A., & Straka, C. W. 2008, Ap&SS, 316, 31

Edvardsson, B., Andersen, J., Gustafsson, B., et al. 1993, A&A, 275, 101

Ferguson, J. W., Alexander, D. R., Allard, F., et al. 2005, ApJ, 623, 585

Foreman-Mackey, D., Hogg, D. W., Lang, D., & Goodman, J. 2013, Publications of the Astronomical Society of Pacific, 125, 306

Formicola, A., Imbriani, G., Costantini, H., et al. 2004, Physics Letters B, 591, 61

Freytag, B., Ludwig, H.-G., & Steffen, M. 1996, A&A, 313, 497

Gaia Collaboration, G., Brown, A. G. A., Vallenari, A., et al. 2016, arXiv.org, arXiv:1609.04172

Gough, D. 1987, Nature, 326, 257

Grevesse, N., & Noels, A. 1993, in 35ème cours de perfectionnement de l'Association Vandoise des Chercheurs en Physique, eds. B. Hauck, S. Paltani, & D. Raboud (AVCP, Lausanne), 205

Grevesse, N., & Sauval, A. J. 1998, Space Sci. Rev., 85, 161

Halbwachs, J. L. 1986, Astronomy and Astrophysics Supplement Series (ISSN 0365-0138), 66, 131

Huber, D., Ireland, M. J., Bedding, T. R., et al. 2012, ApJ, 760, 32

Huber, D., Chaplin, W. J., Christensen-Dalsgaard, J., et al. 2013, ApJ, 767, 127

Iglesias, C. A., & Rogers, F. J. 1996, ApJ, 464, 943

Imbriani, G., Costantini, H., Formicola, A., et al. 2005, The European Physical Journal A, 25, 455

Jimenez, R. 2003, Science, 299, 1552

Johnson, J. A., Huber, D., Boyajian, T., et al. 2014, The Astrophysical Journal, 794, 15

Jontof-Hutter, D., Ford, E. B., Rowe, J. F., et al. 2016, The Astrophysical Journal, 820, 1

Jørgensen, B. R., & Lindegren, L. 2005, A&A, 436, 127

Kippenhahn, R., Weigert, A., & Weiss, A. 2012, Stellar Structure and Evolution:

Kjeldsen, H., & Bedding, T. R. 1995, A&A, 293, 87

Kjeldsen, H., Bedding, T. R., & Christensen-Dalsgaard, J. 2008, ApJ, 683, L175

Lebreton, Y., & Goupil, M. J. 2014, Astronomy and Astrophysics, 569, A21

Lebreton, Y., Perrin, M. N., Cayrel, R., Baglin, A., & Fernandes, J. 1999, A&A, 350, 587

Ledoux, W. P. 1947, ApJ, 105, 305

Lindegren, L., Lammers, U., Bastian, U., et al. 2016, arXiv.org, arXiv:1609.04303

Ludbrook, J. 1997, Clinical and experimental pharmacology & physiology, 24, 193

Lund, M. N., Lundkvist, M., Aguirre, V. S., et al. 2014, Astronomy and Astrophysics, 570, A54

Magic, Z., Serenelli, A., Weiss, A., & Chaboyer, B. 2010, ApJ, 718, 1378

Magic, Z., Weiss, A., & Asplund, M. 2015, Astronomy and Astrophysics, 573, A89

Mathur, S., Metcalfe, T. S., Woitaszek, M., et al. 2012, ApJ, 749, 152

Mazumdar, A., Monteiro, M. J. P. F. G., Ballot, J., et al. 2014, ApJ, 782, 18

McDonald, I., Zijlstra, A. A., & Boyer, M. L. 2012, Monthly Notices of the Royal Astronomical Society, 427, 343

Metcalfe, T. S., Creevey, O. L., Doğan, G., et al. 2014, The Astrophysical Journal Supplement Series, 214, 27

Michaud, G., & Proffitt, C. R. 1993, in In: Inside the stars; Proceedings of the 137th IAU Colloquium, eds. A. Baglin & W. W. Weiss, (Cambridge: Cambridge Univ. Press), Montreal Univ., Canada, 246–259

Miglio, A., & Montalbán, J. 2005, A&A, 441, 615

Miglio, A., Chiappini, C., Morel, T., et al. 2013, MNRAS, 429, 423

Morel, P., & Lebreton, Y. 2008, Ap&SS, 316, 61

Mosumgaard, J. R., Aguirre, V. S., Weiss, A., Christensen-Dalsgaard, J., & Trampedach, R. 2016, arXiv.org, 1610.07323v1

Ng, Y. K., & Bertelli, G. 1998, Astronomy and Astrophysics, 329, 943

Otí Floranes, H., Christensen-Dalsgaard, J., & Thompson, M. J. 2005, MNRAS, 356, 671

Paxton, B., Bildsten, L., Dotter, A., et al. 2011, The Astrophysical Journal Supplement, 192, 3

Paxton, B., Cantiello, M., Arras, P., et al. 2013, The Astrophysical Journal Supplement Series, 208, 4

Paxton, B., Marchant, P., Schwab, J., et al. 2015, The Astrophysical Journal Supplement Series, 220, 1

Pinsonneault, M. H., An, D., Molenda-Żakowicz, J., et al. 2012, The Astrophysical Journal Supplement, 199, 30

Pinsonneault, M. H., Elsworth, Y., Epstein, C., et al. 2014, The Astrophysical Journal Supplement Series, 215, 19

Pont, F., & Eyer, L. 2004, MNRAS, 351, 487

Ramírez, I., Meléndez, J., & Asplund, M. 2009, A&A, 508, L17

Rauer, H., Catala, C., Aerts, C., et al. 2014, Experimental Astronomy, 38, 249

Reese, D. R., Chaplin, W. J., Davies, G. R., et al. 2016, Astronomy and Astrophysics, 592, A14

Rogers, F. J., & Nayfonov, A. 2002, ApJ, 576, 1064

Roxburgh, I. W. 2005, A&A, 434, 665

Roxburgh, I. W., & Vorontsov, S. V. 2003, A&A, 411, 215

Salaris, M., & Cassisi, S. 2015, Astronomy and Astrophysics, 577, A60

Scuflaire, R., Montalbán, J., Théado, S., et al. 2008, Ap&SS, 316, 149

Serenelli, A. M., & Basu, S. 2010, ApJ, 719, 865

Silva Aguirre, V., Ballot, J., Serenelli, A. M., & Weiss, A. 2011a, A&A, 529, 63

Silva Aguirre, V., Chaplin, W. J., Ballot, J., et al. 2011b, ApJL, 740, L2

Silva Aguirre, V., Casagrande, L., Basu, S., et al. 2012, ApJ, 757, 99

Silva Aguirre, V., Basu, S., Brandão, I. M., et al. 2013, ApJ, 769, 141

Silva Aguirre, V., Davies, G. R., Basu, S., et al. 2015, Monthly Notices of the Royal Astronomical Society, 452, 2127

Soderblom, D. R. 2010, ARA&A, 48, 581

Sonoi, T., Samadi, R., Belkacem, K., et al. 2015, Astronomy and Astrophysics, 583, A112

Stassun, K. G., & Torres, G. 2016, The Astrophysical Journal Letters, 831, 1

Steigman, G. 2010, JCAP, 2010, 29

Takeda, G., Ford, E. B., Sills, A., et al. 2007, ApJS, 168, 297

Thoul, A. A., Bahcall, J. N., & Loeb, A. 1994, ApJ, 421, 828

Trampedach, R., Stein, R. F., Christensen-Dalsgaard, J., Nordlund, Å., & Asplund, M. 2014, Monthly Notices of the Royal Astronomical Society, 445, 4366

Ulrich, R. K. 1986, ApJ, 306, L37

Van Eylen, V., & Albrecht, S. 2015, The Astrophysical Journal, 808, 126

van Saders, J. L., Ceillier, T., Metcalfe, T. S., et al. 2016, Nature, 529, 181

Verma, K., Antia, H. M., Basu, S., & Mazumdar, A. 2014a, The Astrophysical Journal, 794, 114

Verma, K., Faria, J. P., Antia, H. M., et al. 2014b, The Astrophysical Journal, 790, 138

Weiss, A., Hillebrandt, W., Thomas, H.-C., & Ritter, H. 2005,
    Cox & Giuli's principles of stellar structure, extended second
    edition, ed. Advances in astronomy and astrophysics
Weiss, A., & Schlattl, H. 2008, Ap&SS, 316, 99

White, T. R., Bedding, T. R., Stello, D., et al. 2011, ApJ, 743, 161
White, T. R., Huber, D., Maestro, V., et al. 2013, MNRAS, 433,
    1262

APPENDIX

A. THE AIMS PIPELINE

The "Asteroseimic Inference on a Massive Scale" (AIMS) pipeline was recently developed at the University of Birmingham in the context of the SpaceInn network. This pipeline relies on various basic components:

- a precalculated grid of models. In the present paper, the grid of main-sequence models from Coelho et al. (2015) was used. This grid of models was calculated via the MESA (Paxton et al. 2013, 2015) stellar evolution code and ranges from $0.8\,\mathrm{M_\odot}$ to $1.5\,\mathrm{M_\odot}$ in steps of $0.01\,\mathrm{M_\odot}$, and from -0.8 dex to 0.8 dex in steps of 0.1 dex for [Fe/H]. The Grevesse & Noels (1993) value of $(Z/X)_\odot = 0.0245$ was used to convert [Fe/H] to Z/X. The enrichment law used $\Delta Y/\Delta Z = 2$ (e.g. Chiosi & Matteucci 1982) and a primordial helium abundance $Y_\mathrm{p} = 0.2484$ (Cyburt et al. 2003). Convection was based on the standard mixing length theory, using a solar-calibrated parameter. No diffusion or rotational mixing was included, while overshoot was taking into account as an adiabatic extension of the mixed region with an efficiency of $d_\mathrm{ov} = 0.20 \times H_\mathrm{p}$. The NACRE thermonuclear reactions are used with the updated rate in $^{14}N(p,\gamma)^{15}O$ from Imbriani et al. (2005)

- the MCMC algorithm from Foreman-Mackey et al. (2013). This provides a way of approximating the probability distribution function in stellar parameter space that results from the provided seismic and classic constraints.

- linear interpolation within the grid of models using a Delaunay tessellation in stellar parameter space (except for the time dimension which is dealt with separately). Hence, AIMS can explore points in parameter space which lie between the stellar models from the grid. The Delaunay tessellation is calculated thanks to the qhull[1] library (via python's numpy library). The advantage of using a Delaunay tessellation is that the grid of models does not necessarily have to be structured.

The AIMS pipeline is freely available[2] along with a more detailed description than what is provided here.

---

[1] See http://www.qhull.org
[2] See http://bison.ph.bham.ac.uk/spaceinn/aims

B. MODELLING INPUT PARAMETERS

In order to determine the stellar properties of our targets each modelling team used the individual frequencies and combinations determined by Lund et al. 2016 (submitted) in the manner described in Section 3. The necessary complementary atmospheric parameters T_eff and [Fe/H] have been compiled from different sources in the literature and listed in Table 3, together with the global asteroseismic quantities.

Simple estimates of $\langle \Delta\nu \rangle$ were obtained using the method of White et al. (2011), that is, from a weighted fit of the asymptotic function $(\nu_0(n) \simeq (n + 1/2 + \epsilon)\Delta\nu)$ to the radial mode frequencies from the peak-bagging as a function of radial order n. The weights were given by a Gaussian with a FWHM of $0.25\nu_\mathrm{max}$. Estimates from a more elaborate method including deviations from the simple asymptotic relation used here can be found in Lund et al. (2016, submitted). The estimate of ν_max was obtained from a Gaussian fit to the radial mode amplitudes from the peak-bagging.

C. CATALOGUES OF STELLAR PROPERTIES

The resulting stellar properties determined by each pipeline are published in the online version of this paper. A description of all fields available is given in Table 4. For the pipelines that do not return asymmetric uncertainties in the stellar properties we report the standard deviation in the positive and negative uncertainties column.

Table B3:. Global asteroseismic and atmospheric properties of our sample.

KIC	$\nu_{\max}$ (μHz)	$\langle\Delta\nu\rangle$ (μHz)	T_{eff} (K)	[Fe/H] (dex)	Reference
1435467	$1406.7^{+6.3}_{-8.4}$	$70.369^{+0.034}_{-0.033}$	6326 ± 77	0.01 ± 0.1	1
2837475	$1557.6^{+8.2}_{-9.2}$	$75.729^{+0.041}_{-0.042}$	6614 ± 77	0.01 ± 0.1	1
3427720	$2737.0^{+10.7}_{-17.7}$	$120.068^{+0.031}_{-0.032}$	6045 ± 77	-0.06 ± 0.1	1
3456181	$970.0^{+8.3}_{-5.9}$	$52.264^{+0.041}_{-0.039}$	6384 ± 77	-0.15 ± 0.1	1
3632418	$1166.8^{+3.0}_{-3.8}$	$60.704^{+0.019}_{-0.018}$	6193 ± 77	-0.12 ± 0.1	1
3656476	$1925.0^{+7.0}_{-6.3}$	$93.194^{+0.018}_{-0.020}$	5668 ± 77	0.25 ± 0.1	1
3735871	$2862.6^{+16.6}_{-26.5}$	$123.049^{+0.047}_{-0.046}$	6107 ± 77	-0.04 ± 0.1	1
4914923	$1817.0^{+6.3}_{-5.2}$	$88.531^{+0.019}_{-0.019}$	5805 ± 77	0.08 ± 0.1	1
5184732	$2089.3^{+4.4}_{-4.1}$	$95.545^{+0.024}_{-0.023}$	5846 ± 77	0.36 ± 0.1	1
5773345	$1101.2^{+5.7}_{-6.6}$	$57.303^{+0.030}_{-0.027}$	6130 ± 84	0.21 ± 0.09	6
5950854	$1926.7^{+21.9}_{-20.4}$	$96.629^{+0.102}_{-0.107}$	5853 ± 77	-0.23 ± 0.1	1
6106415	$2248.6^{+4.6}_{-3.9}$	$104.074^{+0.023}_{-0.026}$	6037 ± 77	-0.04 ± 0.1	1
6116048	$2126.9^{+5.5}_{-5.0}$	$100.754^{+0.017}_{-0.017}$	6033 ± 77	-0.23 ± 0.1	1
6225718	$2364.2^{+4.9}_{-4.6}$	$105.695^{+0.018}_{-0.017}$	6313 ± 76	-0.07 ± 0.1	1
6508366	$958.3^{+4.6}_{-3.6}$	$51.553^{+0.046}_{-0.047}$	6331 ± 77	-0.05 ± 0.1	1
6603624	$2384.0^{+5.4}_{-5.6}$	$110.128^{+0.012}_{-0.012}$	5674 ± 77	0.28 ± 0.1	1
6679371	$941.8^{+5.1}_{-5.0}$	$50.601^{+0.029}_{-0.029}$	6479 ± 77	0.01 ± 0.1	1
6933899	$1389.9^{+3.9}_{-3.6}$	$72.135^{+0.018}_{-0.018}$	5832 ± 77	-0.01 ± 0.1	1
7103006	$1167.9^{+7.2}_{-6.9}$	$59.658^{+0.029}_{-0.030}$	6344 ± 77	0.02 ± 0.1	1
7106245	$2397.9^{+24.0}_{-28.7}$	$111.376^{+0.063}_{-0.061}$	6068 ± 102	-0.99 ± 0.19	4
7206837	$1652.5^{+10.6}_{-11.7}$	$79.131^{+0.037}_{-0.039}$	6305 ± 77	0.10 ± 0.1	1
7296438	$1847.8^{+8.5}_{-12.6}$	$88.698^{+0.040}_{-0.036}$	5775 ± 77	0.19 ± 0.1	1
7510397	$1189.1^{+3.4}_{-4.4}$	$62.249^{+0.020}_{-0.020}$	6171 ± 77	-0.21 ± 0.1	1
7680114	$1709.1^{+7.1}_{-6.5}$	$85.145^{+0.039}_{-0.043}$	5811 ± 77	0.05 ± 0.1	1
7771282	$1465.1^{+27.0}_{-18.7}$	$72.463^{+0.069}_{-0.079}$	6248 ± 77	-0.02 ± 0.1	1
7871531	$3455.9^{+19.3}_{-26.5}$	$151.329^{+0.025}_{-0.023}$	5501 ± 77	-0.26 ± 0.1	1
7940546	$1116.6^{+3.3}_{-3.6}$	$58.762^{+0.029}_{-0.029}$	6235 ± 77	-0.20 ± 0.1	1
7970740	$4197.4^{+21.2}_{-18.4}$	$173.541^{+0.060}_{-0.068}$	5309 ± 77	-0.54 ± 0.1	1
8006161	$3574.7^{+11.4}_{-10.5}$	$149.427^{+0.015}_{-0.014}$	5488 ± 77	0.34 ± 0.1	1
8150065	$1876.9^{+38.1}_{-32.4}$	$89.264^{+0.134}_{-0.121}$	6173 ± 101	-0.13 ± 0.15	4
8179536	$2074.9^{+13.8}_{-12.0}$	$95.090^{+0.058}_{-0.054}$	6343 ± 77	-0.03 ± 0.1	1
8228742	$1190.5^{+3.4}_{-3.7}$	$62.071^{+0.022}_{-0.021}$	6122 ± 77	-0.08 ± 0.1	1
8379927	$2795.3^{+6.0}_{-5.7}$	$120.288^{+0.017}_{-0.018}$	6067 ± 120	-0.10 ± 0.15	2
8394589	$2396.7^{+10.5}_{-9.4}$	$109.488^{+0.034}_{-0.035}$	6143 ± 77	-0.29 ± 0.1	1
8424992	$2533.7^{+27.0}_{-28.1}$	$120.584^{+0.062}_{-0.064}$	5719 ± 77	-0.12 ± 0.1	1
8694723	$1470.5^{+3.7}_{-4.1}$	$75.112^{+0.019}_{-0.021}$	6246 ± 77	-0.42 ± 0.1	1
8760414	$2455.3^{+9.1}_{-8.3}$	$117.230^{+0.022}_{-0.018}$	5873 ± 77	-0.92 ± 0.1	1
8938364	$1675.1^{+5.2}_{-5.8}$	$85.684^{+0.018}_{-0.020}$	5677 ± 77	-0.13 ± 0.1	1
9025370	$2988.6^{+20.0}_{-16.9}$	$132.628^{+0.030}_{-0.024}$	5270 ± 180	-0.12 ± 0.18	3
9098294	$2314.7^{+9.2}_{-10.4}$	$108.894^{+0.023}_{-0.022}$	5852 ± 77	-0.18 ± 0.1	1
9139151	$2690.4^{+14.5}_{-9.0}$	$117.294^{+0.031}_{-0.032}$	6302 ± 77	0.10 ± 0.1	1
9139163	$1729.8^{+6.2}_{-5.9}$	$81.170^{+0.042}_{-0.036}$	6400 ± 84	0.15 ± 0.09	6
9206432	$1866.4^{+10.3}_{-14.9}$	$84.926^{+0.046}_{-0.051}$	6538 ± 77	0.16 ± 0.1	1
9353712	$934.3^{+11.1}_{-8.3}$	$51.467^{+0.091}_{-0.104}$	6278 ± 77	-0.05 ± 0.1	1
9410862	$2278.8^{+31.2}_{-16.6}$	$107.390^{+0.050}_{-0.053}$	6047 ± 77	-0.31 ± 0.1	1
9414417	$1155.3^{+6.1}_{-4.6}$	$60.115^{+0.024}_{-0.024}$	6253 ± 75	-0.13 ± 0.1	7
9812850	$1255.2^{+9.1}_{-7.0}$	$64.746^{+0.067}_{-0.068}$	6321 ± 77	-0.07 ± 0.1	1
9955598	$3616.8^{+21.2}_{-29.6}$	$153.283^{+0.029}_{-0.032}$	5457 ± 77	0.05 ± 0.1	1
9965715	$2079.3^{+9.2}_{-10.4}$	$97.236^{+0.041}_{-0.042}$	5860 ± 180	-0.44 ± 0.18	3
10068307	$995.1^{+2.8}_{-2.7}$	$53.945^{+0.019}_{-0.020}$	6132 ± 77	-0.23 ± 0.1	1
10079226	$2653.0^{+47.7}_{-44.3}$	$116.345^{+0.059}_{-0.052}$	5949 ± 77	0.11 ± 0.1	1
10162436	$1052.0^{+4.0}_{-4.2}$	$55.725^{+0.035}_{-0.039}$	6146 ± 77	-0.16 ± 0.1	1
10454113	$2357.2^{+8.2}_{-9.1}$	$105.063^{+0.031}_{-0.033}$	6177 ± 77	-0.07 ± 0.1	1
10516096	$1689.8^{+4.6}_{-5.8}$	$84.424^{+0.022}_{-0.025}$	5964 ± 77	-0.11 ± 0.1	1
10644253	$2899.7^{+21.3}_{-22.8}$	$123.080^{+0.056}_{-0.055}$	6045 ± 77	0.06 ± 0.1	1

Table C4:. Stellar properties for the LEGACY dwarfs sample determined by each pipeline. All tables are available in the machine readable format in the online version of this paper. Fields are given here for guidance regarding its form and content.

Field	Description
KIC	*Kepler* Input Catalogue Identifier
Mass	Mass in solar units
sMassP	Positive mass uncertainty in solar units
sMassM	Negative mass uncertainty in solar units
Rad	Radius in solar units
sRadP	Positive radius uncertainty in solar units
sRadM	Negative radius uncertainty in solar units
Grav	Surface gravity in dex
sGravP	Positive surface gravity uncertainty in dex
sGravM	Negative surface gravity uncertainty in dex
Age	Age in units of Gyr
sAgeP	Positive age uncertainty in units of Gyr
sAgeM	Negative age uncertainty in units of Gyr
Lum	Luminosity in solar units
sLumP	Positive luminosity uncertainty in solar units
sLumM	Negative luminosity uncertainty in solar units
Rho	Density in g/cm^3
sRhoP	Positive density uncertainty in g/cm^3
sRhoM	Negative density uncertainty in g/cm^3
Dist	Distance in pc
sDistP	Positive distance uncertainty in pc
sDistM	Negative distance uncertainty in pc
Xini	Fractional initial hydrogen abundance
sXiniP	Positive fractional initial hydrogen abundance uncertainty
sXiniM	Negative fractional initial hydrogen abundance uncertainty
Yini	Fractional initial helium abundance
sYiniP	Positive fractional initial helium abundance uncertainty
sYiniM	Negative fractional initial helium abundance uncertainty
Xsup	Fractional surface hydrogen abundance
sXsupP	Positive fractional surface hydrogen abundance uncertainty
sXsupM	Negative fractional surface hydrogen abundance uncertainty
Ysup	Fractional surface helium abundance
sYsupP	Positive fractional surface helium abundance uncertainty
sYsupM	Negative fractional surface helium abundance uncertainty
Xcen	Fractional central hydrogen abundance
sXcenP	Positive fractional central hydrogen abundance uncertainty
sXcenM	Negative fractional central hydrogen abundance uncertainty
Ycen	Fractional central helium abundance
sYcenP	Positive fractional central helium abundance uncertainty
sYcenM	Negative fractional central helium abundance uncertainty
MCcore	Mass coordinate of the convective core edge
sMCcoreP	Positive fractional uncertainty in mass coordinate of convective core edge
sMCcoreM	Negative fractional uncertainty in mass coordinate of convective core edge
Rbce	Radius coordinate of the base of the convective envelope
sRbceP	Positive fractional uncertainty in radius coordinate of the base of the convective envelope
sRbceM	Negative fractional uncertainty in radius coordinate of the base of the convective envelope
α_{conv}	Convective efficiency
$s\alpha_{conv}P$	Positive fractional uncertainty in convective efficiency
$s\alpha_{conv}M$	Negative fractional uncertainty in convective efficiency
TAMS	Terminal age main sequence

NOTE—Asymmetric uncertainties are given when available, otherwise the standard deviation of the property is given in the positive and negative uncertainty fields. Density uncertainties for the C2kSMO results are not reported, while convective efficiencies and TAMS values are not available for all pipelines (see Section 4.1 for details).